ACS OMEGA

http://pubs.acs.org/journal/acsodf

Article

Morphological and Semi-empirical Study of the Pluronic F68/Imogolite/Sudan III Intersurfaces Composite for the Controlled Temperature Release of Hydrophobic Drugs

Vicente D. Samith,* Sebastián Navarro, and Reza Dabirian

Cite This: *ACS Omega* 2020, 5, 20707−20723

Read Online

ACCESS | Metrics & More | Article Recommendations

ABSTRACT: Some PluronicF68 (F68) triblock copolymer properties demonstrate surprising applications in selective drug administration, such as the transportation of hydrophobic anti-inflammatories through epithelial barriers. Nuclear magnetic resonance (^{1}H-NMR) spectroscopy was carried out for micelle precursor dispersions and F68 films modified with a synthetic imogolite (IMO) biocompatible hydrogel. Theoretical calculations and morphological assessment for the process of morphogenesis of dendritic crystallization were performed by molecular docking and atomic force microscopy (AFM) of the Sudan III-IMO-F68 composite, which was more hydrophobic than Sudan III-F68 and carried out the prolonged release of the Sudan III "drug" captured by a water−octanol interface determined by standard absorbance. Surface fusions were measured and compared to the unmodified matrix. However, despite the superior properties of the composite, the critical micelle concentration (CMC) was practically unmodified because solitary IMO strands attached to Sudan III formed Sudan III-IMO. These strands unraveled in a stable manner by expanding like a "spiderweb" in hydrophilic interfaces according to NMR analysis of the hydrogen one H_1 polarization of Sudan III and F68 methyl, whose correlation relates hydrophobicity of Sudan III-IMO-F68 with dendrite properties from F68 concentrations. CMC and surface fusions equivalent to F68 surface properties, calculated by differential scanning calorimetry and dynamic Raman spectroscopy, were determined by AFM and high-resolution ellipsometry. Our results show highly specialized pharmacological applications since micelle surfaces expand, triggering maximum deliveries of "Drugs" from its interior to the physiological environment. The implanted sensor prototype determined equilibria reached Sudan III according to temperature (32−50 °C) and time it took to cross the membrane model 1-octanol (48 h). The findings suggest that the targested design of a F68-IMO-"Drug" would function as a microdevice for the prolonged release of hydrophobic drugs. In addition, the said microdevice could regenerate the damaged tissue in the central nervous system or other organs of the body. This is due to the fact that it could perform both tasks simultaneously, given the properties and characteristics acquired by the compatible material depending on the temperature of the physiological environment.

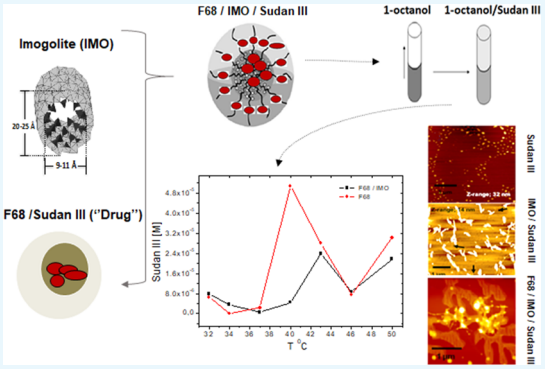

INTRODUCTION

The search for systems capable of delivering drugs in a controlled and safe manner has led researchers to develop various materials capable of performing that role.[1,2] However, these substrates should fulfill a number of conditions to ensure high efficiency in the release of drugs in the therapeutically required dose for successful treatment, decreasing possible undesired interactions, so factors such as size and load play a critical role during the process of release.[3]

Some of the materials that have been widely used in the pharmaceutical industry as active ingredients or excipients are clays, which provide, due to their properties (surface area and load, sizes, and adsorption capacity, among others), the possibility of achieving controlled release by an ion exchange process.[2,4] In this process, the ions present in the biological fluids, through a mass effect or affinity with the clay, can release the adsorbed drug.[5] Figure 1 shows the structure of imogolite, a nanotubular aluminosilicate present in volcanic soils, whose synthesis was developed, that has been gaining increasing interest due to its high chemical versatility, which makes it a potential candidate as a controlled drug release system.[6]

Received: September 11, 2019
Accepted: March 3, 2020
Published: August 13, 2020

https://dx.doi.org/10.1021/acsomega.9b02965
ACS Omega 2020, 5, 20707−20723

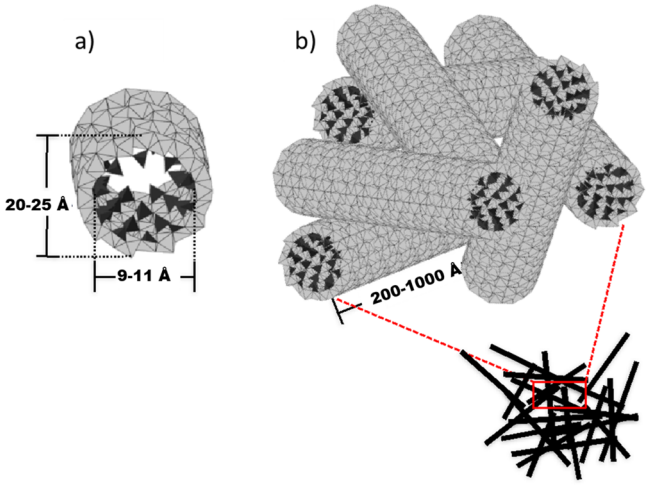

Figure 1. Dimensions of imogolite nanotubes and their possible spatial distribution. (b) Imogolite structure. (a) F68 inside of the imogolite estructure.

The chemical formula of imogolite is $(OH)_3Al_2O_3SiOH$, and it is characterized by hollow cylindrical structures with an average outer diameter of 2.5 nm (~20−25 Å), an average internal diameter of 1.5−2.0 nm (~9−11 Å), and a length that varies from 100 nm to several micrometers.[7,8] These nanotubes have an outer surface where aluminol groups (≡Al—OH and $\equiv Al_2$—OH) predominate, and they are mostly responsible for the isoelectric point of imogolite (IEP ≈ 10.5), facilitating the adsorption of anions.[9] The inner surface is enriched with silanol groups (≡Si—OH), which are isolated. On this surface, cation adsorption is dominant over a wide pH range, but the inner diameter of imogolite hinders their diffusion. In spite of adsorbing cations and anions simultaneously, anion adsorption is predominant on imogolite.[9] It has been reported that the extensive network of "hollow" IMO nanofibers in a "spiderweb" arrangement has a great ability for trapping a variety of molecules in large amounts due to its particular architecture.[10]

Because of its physicochemical properties, new hybrid materials based on imogolite and polymers have been developed with different optical, electric, and mechanical properties.[11] Research on the interaction of imogolite with macromolecules has allowed the development of hybrids of the imogolite-DNA and imogolite-RNA type, whose stability is due mainly to the strong interaction of the aluminol groups with the phosphate groups that are constituents of these nucleic acids, yielding materials that have biomedical applications.[12]

Although research done with imogolite in the field of controlled drug release is almost nonexistent, the physicochemical, structural, and surface properties, together with their biological innocuousness, make these nanotubes excellent candidates for these kinds of studies.[13] Because of their qualities, imogolite nanofibers have been chosen as a novel three-way reservoir-transporter-deliverer of lipophilic drugs. A new composite material based on a pluronic acid[14] is introduced, Sudan III-Imogolite-Pluronic-F68[15] (Sudan III-IMO-F68), and it provides the compound with the properties and characteristics of both components. This is according to the proportion of each of them in the compatibilized material (see Experimental Methods). It is obtained directly from the triblock poly(ethyleneoxide)-poly(propylene oxide)-poly(ethylene oxide) copolymer (Pluronic F68 (PEO_{76}-PPO_{29}-PEO_{76})), which belongs to a class of biocompatible nonionic amphiphilic surface-active compounds that have applications in medicine,[15,16] including drug transport and incorporation at desired targets in the human body[17,18] or in other kinds of biological systems. In such a direction, triblock copolymers are composed of three or more covalently linked polymers, which possess different physicochemical properties. Amphiphilic block copolymers spontaneously assembly form micelles, which has a hydrophobic core surrounded by a hydrophilic shell in aqueous medium depending on parameters such as chemical structure, composition, and concentration.[19−23]

Pluronic F68 was chosen because it is a nonionic amphiphilic tensioactive approved by the FDA that satisfies the desired requirements: (i) excellent cellular sealer[24,25] with many applications in the fields of regenerative biology[16,26] and (ii) a vehicle for the controlled release of drugs, especially lipophilic drugs.[27] On the other hand, F68 in water solution has a very singular physicochemical behavior, mainly in the critical micelle concentration (CMC) interval.[14,15,24,28] The CMC intimately related to the percentage coverage of the 2D crystal structures that are formed on the SiO_x substrate. Interestingly, above the CMC the dendritic types of microaggregates will depend on the concentration of Pluronic F68.[15,29−31] Consequently, the device "Drug"-IMO-F68 (Sudan III-IMO-F68) based on the F68 matrix would have pharmacological properties and controlled release of hydrophobic drugs[15] or other active agents depending on the temperature. Estimation of the CMC and its correlation with the morphology (F68 dendritic types of microaggregates) increases cell viability of a human neuronal model in vitro (F68), thus aim CMC estimation. Also, the molar concentration F68 correlation increases cell viability of a human neuronal model in vitro. In this way, the CMC coincides with neuronal viability maximum of human neuroblastoma SH-SY5Y cells (incubated with F68 for 24 h analyzed by MTT assay[15]).

On the other hand, the carrying capacity of Sudan III (hydrophobic drug model: "drug") into F68 micelles in aqueous medium and human plasma it has been proven. In this sense, maximum cell viability is related to the CMC, maximum surface tension (F68 aqueous solution), and maximum percentage coverage area of F68 on SiO_x (simplified model of the hydrophilic surface of cell membranes[15]). According to the previous observations, the CMC of F68 regarding morphology, surface tension, and cell viability showed important changes that are consistent with the modification of penetration performance into the plasma membrane. Likewise, the solid bulk material will behave similarly, forming micelle macroaggregates that are self-assembled in solution. So, dispersions formed depend on the added amounts of such a surfactant in a given volume and temperature.[32,33]

In this work, the micro- and macroscopic properties of block copolymers are expected to improve the "drug" release process (Sudan III), which will be deeply affected by the properties of the material. These forms can increase the amount of "drug" that can be encapsulated in the microaggregates formed by amphiphilic triblock copolymers compatible with imogolite fibers. Therefore, the characterization of the physical−chemical phenomena in the micellar systems will maximize the carrying capacity and prolong the controlled release of the hydrophobic drug toward a specific objective,[34] such as the central nervous system, damaged tissues, etc. In addition, the sorption capacity

https://dx.doi.org/10.1021/acsomega.9b02965
ACS Omega 2020, 5, 20707−20723

and solubility of imogolite nanotubes (internal diameter, ∼1.5−2.0 nm) and their adhesion (external diameter, ∼2.5 nm) in the micelles of the F68 matrix (hydrophilic shell and hydrophobic core of the F68 micelles) will be better at physiological temperatures. A new microdevice material capable of controlling drug release was designed. To this end, an imogolite-modified triblock amphiphilic copolymer will be characterized in the controlled release of a hydrophobic drug in solution.[34]

Therefore, a study of the phenomenological, physicochemical, and morphological behavior of micelles was carried out by trapping and releasing the hydrophobic drug. A device model was designed, which optimizes the absorption and release of the "drug" as a function of temperature in an environment that emulates a simplified physiological medium.

The morphological characteristics of the material were analyzed by atomic force microscopy (AFM: tapping mode and contact mode[15,31,36]). The fusion of the matrix material F68 was analyzed by differential scanning calorimetry (DSC[41]) and Raman spectroscopy as a function of temperature.[40] These studies contrast with the ^{1}H-NMR[35,37−39] correlations that explain the hydrophobicity indices for the systems and components involved. The determination of the CMC of F68 was performed by high-resolution eliposometry[37,42] for films on the hydrophilic substrate. Additionally, theoretical calculations were performed in accordance with "Molecular Docking" components corresponding to independent parts of each system studied:[43,44] Sudan III-IMO, Sudan III-F68, IMO-Sudan III, IMO-F68, and Sudan III-IMO-F68. The theoretical and experimental behavior of the new material Sudan III-IMO-F68 compared to Sudan III-F68 is consistent in a biphasic system on temperature. That is, where Sudan III ("drug") is collected and measured into 1-octanol by standard absorbance in the process prolonged release of hydrophobic "drug": aqueous dispersion/1-octanol[45,46] acts as a simple model of a membrane cellular biologic medium (simplified physiological medium), which is explained formally on temperature.

EXPERIMENTAL METHODS

Synthesis of Aluminosilicate Nanotubes. The imogolite was synthesized using the procedure described by Mukherjee et al.[47] Tetraethyl orthosilicate (TEOS) solution was added to an aqueous solution containing 5 mM $AlCl_3$ until a 2:1 Al/Si ratio was achieved. Then, a 0.1 M NaOH solution was added slowly to get an OH/Al ratio close to 2. The mixture was stirred overnight and heated in an oven at 95 °C for 5 days. Once the aging process had ended, the resultant mixture was cooled to ambient temperature. The suspension was concentrated by centrifugation at 9000 rpm for 30 min and subsequently washed with deionized water until its electric conductivity was below 0.78 $dS{\cdot}m^{-1}$.

Silicon Substrates. Crystalline Si(100) wafer (0.4 mm-thick, Virginia Semiconductor, Inc.) were coated with native SiO_2 oxide of <12 Å thickness, measured by X-ray reflection.[30,36]

Silicon Substrate Cleaning. Before the analyses, the silicon was cleaned by immersing it in a mixture of sulfuric acid and hydrogen peroxide (70% H_2SO_4 + 30% H_2O_2) at 90 °C for 30 min. The substrates were stored in ultrapure water (Merck) and then dried in a dry nitrogen stream. This procedure, which does not remove the native oxide layer, produces substrates with a very reproducible hydrophlic surface.[48]

Spin-Coating and Drop-Casting. Control of the self-assembly of the materials studied at the nano- and microscale on silicon was carried out by depositing the solution aliquots that contain the component materials using the spin-coating technique. Immediately, the spinning rate (2000 rpm) was applied during a period of time (spin-coating method) shown in which it produces a uniform film that covers the surface of the substrate. The other technique used for the deposition of the solutions is the direct addition of a drop of a known volume on the surface of the substrate.[29] The sample was dried immediately with nitrogen at ambient temperature, forming the film concentrically on the surface as the drying process described took place.[29,36]

Preparation of Films on SiO_x. The films of imogolite hydrogel, Sudan III, and both components on SiO_x at ambient temperature were prepared (Figure 2). Precipitation of a 10 μL

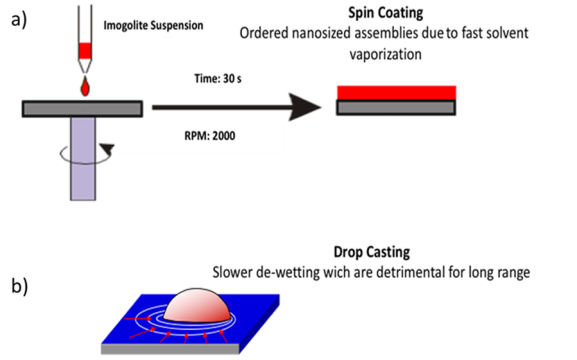

Figure 2. Schematic representation of the (a) spin-coating and (b) drop-casting processes.

imogolite aliquot (drop) with a concentration of 12 mg/mL on the substrate was carried out by drop-casting. Preparation of the imogolite-Sudan III (Sudan III-IMO) complex on the substrate was carried out in two successive stages: deposition of a 10 μL drop of a 0.1 mg/mL solution of Sudan III in tetrahydrofuran (THF) (Merck) (deposited by spin-coating at 2000 rpm for 60 s on the substrate). On the formed film, a 10 μL drop of a 12 mg/mL solution of imogolite hydrogel was deposited by spin-coating at 2000 rpm for 60 s. The third and last stage is deposition of a 10 μL drop of a 0.65 mg/mL aqueous solution of Pluronic F68 (F68) on the substrate spin-coating (it immediately) at 3200 rpm for 60 s.[49] The scheme on the right represents the deposition of a 10 μL drop of a 12 mg/mL aqueous solution of the Sudan III-imogolite (Sudan III-IMO) complex containing 0.1 mg of Sudan III (Aldrich), which was applied by drop-casting on the previously formed film (Figure 2).

AFM in Tapping Mode. By means of an AFM NTEGRA Prima System (NT-MDT (Russia)), semicontact or intermitent contact (tapping) measurements were made with a standard 300 kHz silicon probe. The sample preparation of the thin films used for AFM has been explained in detail in the previous part of this section.

Preparation of Micellar Solutions. Nanopure water was used to prepare the micellar solutions. A 32% (w/v) stock solution of Pluronic F68 (Aldrich) was used to prepare the corresponding dispersions of Sudan III-F68 and Sudan III-IMO-F68. Sudan III (Aldrich) was dissolved in a 10^{-3} M concentration of a dispersion that contains 250 μL of THF, and it was added to 500 μL of both dispersions, with constant

https://dx.doi.org/10.1021/acsomega.9b02965
ACS Omega 2020, 5, 20707−20723

stirring in 1 mL tubes at 37 °C until complete evaporation of the organic solvent.[15,29]

^{1}H-NMR Spectroscopy. ^{1}H-NMR spectra were taken with a BRUKER AVANCE spectrometer operating at a ^{1}H frequency of 400 MHz. The samples were dissolved in DMSO-d_6 (99.8% minimum degree of deuteration for NMR spectroscopy) to provide an internal chemical shift standard (Merck) at 2.5 ppm. One-dimensional ^{1}H spectra were run in 5 mm diameter NMR tubes, scanning 1024 points in the time domain, with a spectral width of 4200 Hz. The spectra were obtained at room temperature. Data processing and ^{1}H peaks were carried out using XWIN-NMR software.

Molecular Simulation. Configurational optimization and prediction of the free energy of the interactions involved in materials that have multiple degrees of freedom can be approximated satisfactorily in the complex systems. The simplified global systems were calculated computationally by means of an empirical function of points (Score) and a coupling vector (shape of a spring) in the ArgusLab program[X] with a Dock coupling protocol (score/shape). In this way, all the energy minima of the simulated systems are explored formally.[43]

Determination of Sudan III in the 1-Octanol Phase. A 0.5 mL volume of 1-octanol (Merck) was added to complete 1 mL in pairs of tubes that contain the aqueous dispersions of Sudan III-F68 and Sudan III-IMO-F68. After 48 h at each temperature (at which both sets had been), the 1-octanol phase[46,50] that contained the Sudan III was collected, and it was analyzed spectrophotometrically at 511 nm using a UV−visible detector (Visible Spectrophotometer HALO VISs-10, Dynamica[15,28]). The scheme in Figure 9a represents the distribution process from the aqueous dispersion to the 1-octanol phase. The Sudan III-IMO complex is represented on the left. It is incorporated to the micelles of Pluronic F68 (F68) by compatibilization, encapsulating the cores of aggregates of Sudan III molecules trapped in "a spiderweb network" of Sudan III-IMO in the micelles of Sudan III-IMO-F68. Similarly, the micelles of F68 show solubilize Sudan III in the hydrophbic core. The transfer of Sudan lII to the 1-octanol organic phase, from both systems after 48 h as a function of temperature, is represented on the right.

Differential Scanning Calorimetry (DSC). Prior to carrying out the thermal process, the Pluronic F68 (F68) samples were dried under reduced pressure. They are heated to the high temperature limit from 25 to 100 °C and then cooled rapidly with liquid nitrogen in a Mettler Toledo DSC calorimeter. The melting temperature was then determined in the 25−100 °C range at a heating rate of 20 °C/min in a nitrogen atmosphere.[51,52]

Raman Spectroscopy. The melting processes of Pluronic F68 (F68) were determined by means of two thermal cycles in the 25−100 °C temperature range, with a precision of ±0.1 °C, from the Raman spectra obtained on a LabRam010de ISA instrument with a 5.5 mW HeNe laser (633 nm) without a filter. A Linkam TMS94/THMS 600 controller was used to change the sample's temperature at a rate of 10 °C/min.[53,54] To guarantee the sample/sample holder thermal equilibrium, the temperature was stabilized for 1 min before running each spectrum.[40,51,55]

High-Resolution Ellipsometry of F68 on Silicon (SiO_x). Aliquots of 30 μL of aqueous solutions of Pluronic F68 at concentrations of (0.5, 2.0, 6.0, 10.0, 20.0) × 10^{-4} M were added by drop-casting to the SiO_x substrate. High-resolution ellipsometry was used to measure three successive heating−cooling cycles (up and down) of each of the films formed on SiO_x.[36] The samples were measured successfully by registering the polarization angle changes (δP) as a function of temperature (25−90 °C). The ellipsometer used in the experiment consists of a conFiguredor PCSA (polarizer, compensator, sample-analyzer). Through the polarizer and the compensator, the laser beam reaches the sample's film surface at an angle of incidence of 60°, illuminating a ∼1 mm^2 area. The reflected light passes through an analyzer and then enters the photodetector (which has a telescope focused on the illuminated sample area), which diffuses the light isotropically from the film. The parasitic light intensity is measured with a photomultiplier and the position of the polarizer (which is proportional to the optical width of the film formed on the SiO_x), and it is controlled automaticaly with a feedback loop with a resolution of 0.001° (corresponding to ∼0.02 Å[29,36]).

AFM Analysis in Contact Mode and Tapping Mode of F68 on Silicon. The thin films prepared by drop-casting at concentrations of (0.5, 2.0, 6.0, 10.0, 20.0) × 10^{-4} M were analyzed by contact mode AFM at 25 °C. The samples prepared by spin-coating with concentrations of (0.5, 2.0, 6.0, 10.0) × 10^{-4} M were analyzed by AFM in tapping mode at 25 °C[49] (Figure 2).

RESULTS

AFM Analysis. The previous FTIR, XRD, and TEM characterizations of the synthetic imogolite nanofibers were described. The FTIR spectra of the imogolite showed the characteristic signals of imogolite at 487, 537, 723, 990, and 939 cm^{-1}, belonging to the Si−O stretching vibrations, which are specific of tubular structures. The hydroxyl region shows the presence of three kinds of signals, which are distinguished at 3300, 3500, and 3615 cm^{-1}. These are corresponding to hydroxyl associated to Al and Si (≡AlOH, ≡Al_2OH, and ≡Si—OH). Accordingly, for synthetic imogolite, the XRD pattern exhibits four diffuse bands at 21.0, 12.0, 3.4, and 2.2 Å.

Observation of solid imogolite samples shows that the spatial distribution of imogolite nanotubes is similar to a spiderweb, which would explain their great adsorption capacity. The dimensions of synthetic imogolite have been shown lengths to exceed ∼200 nm, after verifying in the SEM images. On the other hand, the studies carried out by TEM show an external diameter of ∼2.5 nm and an internal diameter of ∼1.5−2.0 nm for synthetic imogolite[8,9] (Figure 1). In agreement with the topology analyzed by AFM, Figure 3a shows a network of nanofibers covering the substrate, with lengths that easily exceed 200 nm. The longitudinal white line in the AFM image in Figure 3b represents the cross section of the film along the position (μm) in the graph of Figure 3c with heights that go from ∼10 to ∼20 nm. The larger ones (∼20 nm) correspond to granules of the material that are distributed over the fibers with an altitude of ∼2.5 nm.

The dispersion imogolite (IMO), applied on the molecular aggregates molecules of Sudan III dispersed over the SiO_x in Figure 4a,b, forms a nanofiber structure that self-assembles, forming cumuli of Sudan III indicated by black arrows in Figure 4c,d. These are trapped and threaded in a "spiderweb" adhered to the substrate. The AFM images in Figure 4f,g show in detail the organization of the nanofilaments inserted in the cores of molecules of Sudan III that have been added in the assembly process.

https://dx.doi.org/10.1021/acsomega.9b02965
ACS Omega 2020, 5, 20707−20723

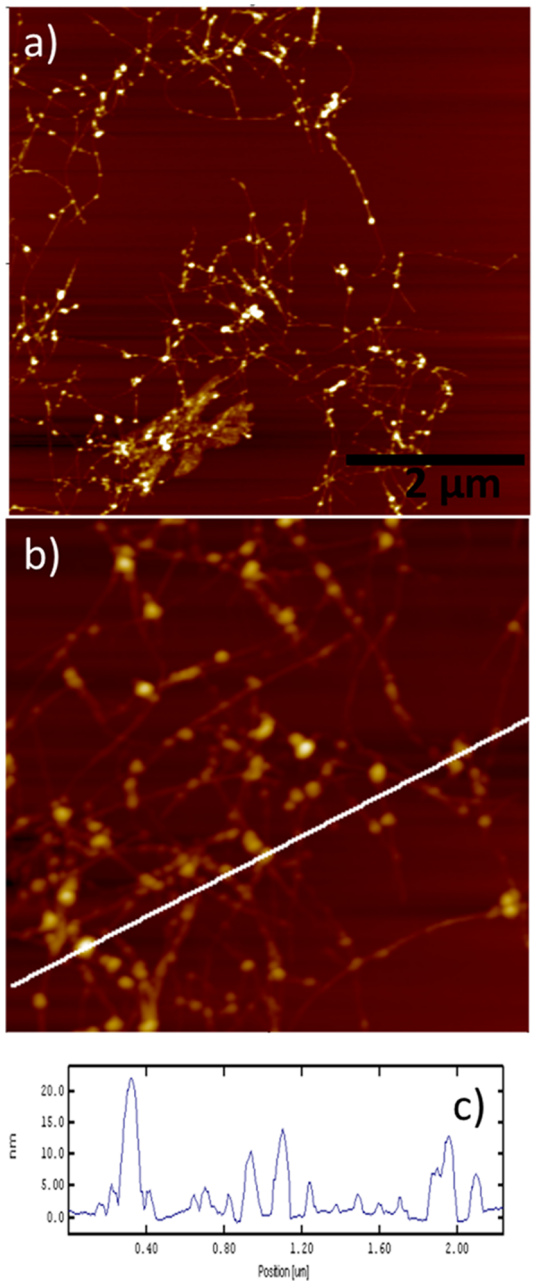

Figure 3. AFM images (spin-coating technique) of the imogolite nanotubes adsorbed on a mica surface. (a) Film of synthetic imogolite fibers (b). Cross section (white line) and (c) profile of the film.

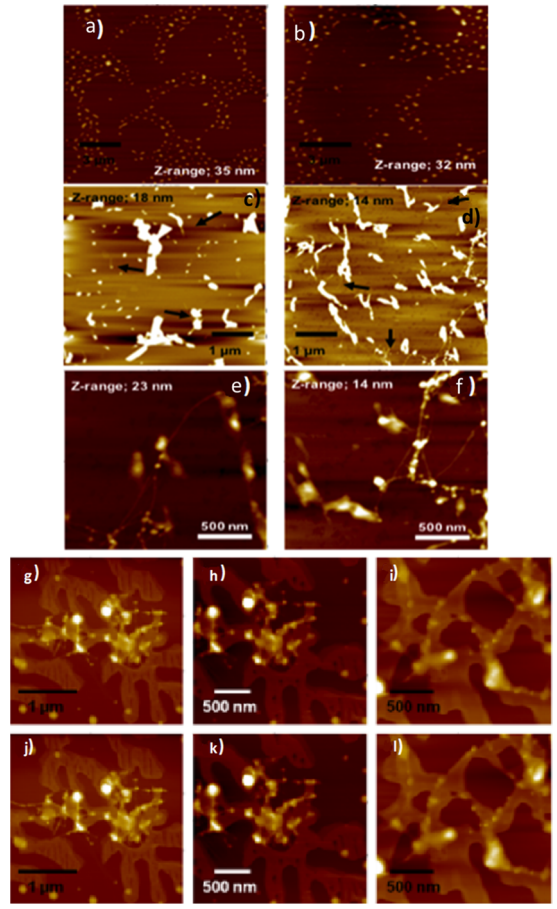

Figure 4. AFM images in scanning mode technique on mica (spin coating). (a, b) Anhydrous Sudan III dispersed regularly on the surface of the mica substrate. (c, d) The IMO fibers always initiate from the Sudan III structures (hydrated aggregated molecules), either as bridges between the agglomerates or as solitary fibers (IMO) (the nanofibers are never found "alone" in the sample) (black arrows). (e, f) Amplification of the complex formed by nanofibers and cores of aggregated Sudan III (Sudan III-IMO). (g–l) Sudan III-IMO complex arranged on the dendritic surface F68: amplified structure (detail: (i) and (l)) of the Sudan III clusters is implanted in the IMO fibers, forming a mesh anchored into F68 dendritic matrix.

The set of AFM images in Figure 4c–l shows that the network composed of nanothreads of Sudan III-IMO is anchored to the dendritic sheets of F68 on the substrate. The image on the left shows a compact reticular palisade, supported by interconnections of fibers, threaded to the percentage coverage 2D crystal flat sheets structures (dendrites) of F68 that compose the Sudan III-IMO-F68 film on the SiO_x substrate.

^{1}H-NMR Spectroscopy of Sudan III-IMO and Sudan III-IMO-F68. The systematic study of Sudan III in Figure 5a for the respective Sudan III, Sudan III-IMO, and Sudan III-IMO-F68 dipersions (dissolved in DMSO-d_6) in Figure 5b shows the spectra of the hydrogen in the molecule of Sudan III. The spectra corresponding to the aromatic hydrogens H_1 of the Sudan III molecule are indicated (black polygon). Every chemical shift $\Delta\delta$ Hz corresponds to a system with respect to Sudan III, as shown in Table 1.

The main character is H_1, which presents significant high-field resonant energies in the following increasing order: Sudan III-F68, Sudan III-IMO, and Sudan III-IMO-F68, with chemical shifts, $\Delta\delta$ Hz, of 13.685, 11.710, 7.620, and 5.910, respectively. The last two correspond to the signal presented in detail as a "double peak" constituted by the pair of hidden signals (Figure 5b and Table 1), which are relatively displaced to higher fields with respect to the H_1 of the hydrophobe Sudan III.

Also, the spectra of Figure 5c summarized in Table 2 represent the chemical shifts of the methyl group ($-CH_3$) of block propylene polyoxide (PPO) of F68 relative to that in Sudan III-F68, Sudan III-IMO-F68, and IMO-F68. The former is displaced to high field $\Delta\delta$ = 10.560 Hz followed by the displacements to low fields of $\Delta\delta$ = −4.250 Hz and $\Delta\delta$ = −3.840 Hz, respectively.

Molecular Docking. The molecular simulation optimizes structurally the experimental systems of the previous point in

https://dx.doi.org/10.1021/acsomega.9b02965
ACS Omega 2020, 5, 20707−20723

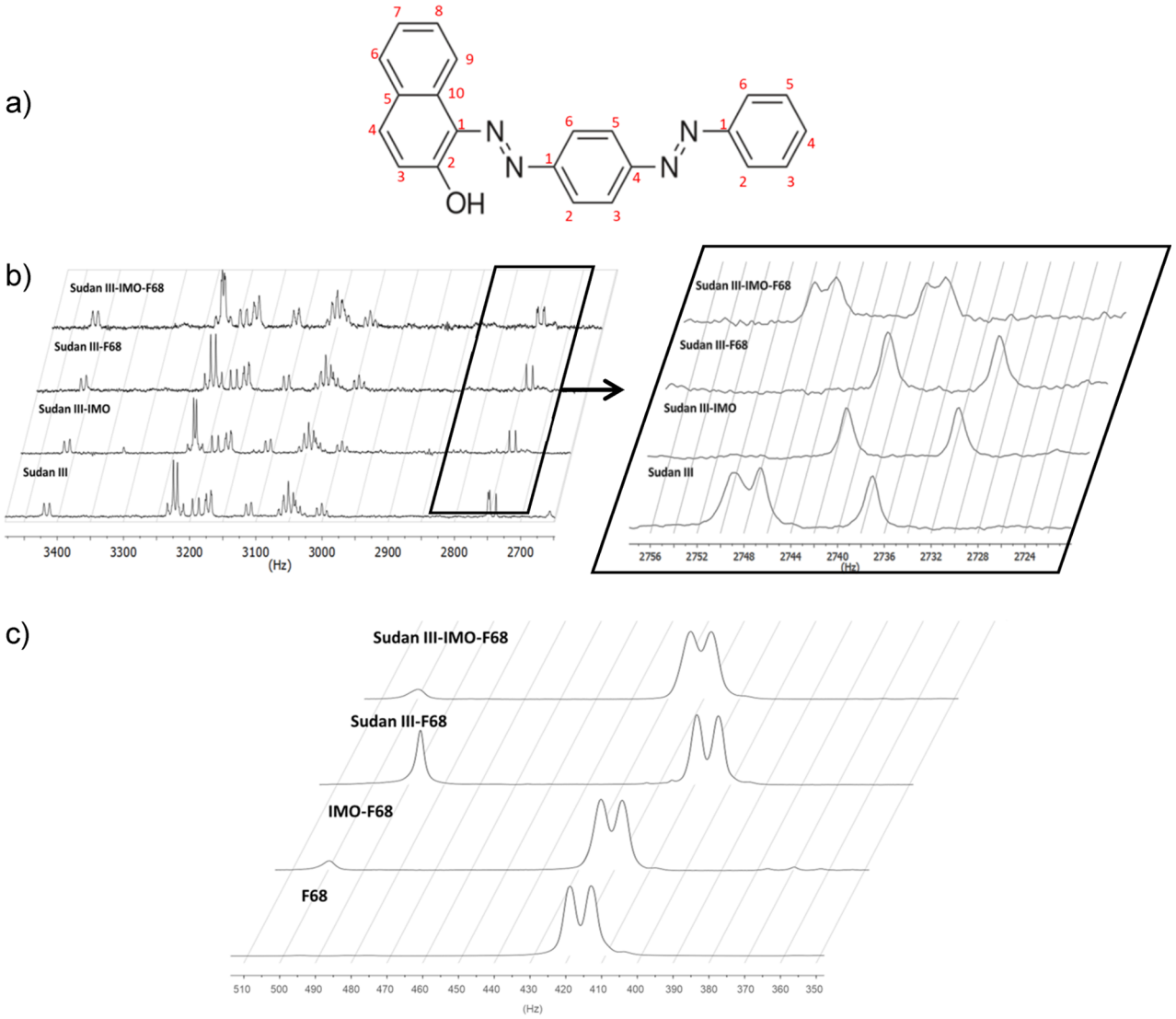

Figure 5. (a) Structure hydrophobic molecules Sudan III and the hydrogens numbered from H_1 to H_{15} (H_1 is encircled in red). (b) ^{1}H-NMR spectra (Hz) of the hydrogens (Table 1) of Sudan III, Sudan III-IMO, Sudan III-F68, and Sudan III-IMO-F68. H_1 of Sudan III and Sudan III as a component of each system (blue polygon). An enlarged view of the H_1 spectrum (black polygon) (right) details its behavior (Hz) in each system. (c) Signals of the ^{1}H-NMR (Hz) spectra of the methyls (Table 2) of the PPO (F68) block in the systems in solution: F68, Sudan III-F68, and Sudan III-IMO-F68.

Table 1. Maximum of the Spectral Signals ^{1}H-NMR of Hydrogen, H_1 δ (Hz), of Sudan III Belonging to the Systems in Relation to Hydrogen, H_1 δ (Hz), of Sudan III Belonging to the Systems, Whose Difference Is $\Delta\delta$ (Hz)

system	H_1 δ Hz	H_2 δ Hz	H_3 δ Hz	H_4 δ Hz	H_5 δ Hz	H_6 Hz	$H_{7\text{-}8\text{-}9\text{-}10}$ δ Hz	$H_{11\text{-}15}$ δ Hz	$H_{12\text{-}13\text{-}14}$ δ Hz
Sudan III	2747.61	3190.74	3110.58	3415.67	3000.31		3221.4	3171.15	3050.76
Sudan III-IMO	2735.9	3185.13	3105.13	3408.91				3164.4	3046.64
$\Delta\delta$	11.71	5.61	5.45	6.76				6.75	4.12
Sudan III-F68	2733.93	3180.94	3101.21	3407.6	2991.43		3211.86	316.,72	3041.9
$\Delta\delta$	13.68	9.8	9.37	8.07	8.88		9.54	9.43	8.86
Sudan III-IMO-F68	2739.99	3189.73	3110.07	3413.51	2992.67		3220.37	3169.81	3049.53
$\Delta\delta$	7,62	1.01	0.51	2.16	7.64		1.03	1.34	1.23

Figure 6a–d. Table 3 shows approximations that correspond, in this case, to the energy involved in those interactions (ΔG_I kcal/mol) in each system (the asterisk (*) corresponds to the parts of the simulated compounds) (Figure 6a). In this way, a cross-sectional cut of imogolite (IMO) through the IMO* molecular ring interacts with a molecule of Sudan III*, forming the Sudan III*-IMO* complex with an energy difference of $\Delta G_I = -4.40$ kcal/mol, which represents the formation energy of the complex. On the other hand, the $[(EO)_2\text{-}(PO)\text{-}EO)_2]$ [(ethylene oxide)$_2$-(propylene oxide)-(ethylene oxide)$_2$] (F68*) dimer is a simplified version of a part of F68 that interacts with IMO* (Figure 6b) and Sudan III* (Figure 6c)

https://dx.doi.org/10.1021/acsomega.9b02965
ACS Omega 2020, 5, 20707−20723

Table 2. Maximum of the Spectral Signals ^{1}H-NMR δ (Hz) of the $-CH_3$ (PPO) Group of F68 in Relation to, δ (Hz), of the $-CH_3$ (PPO) Groups of F68 Corresponding to the Systems, Whose Difference Is $\Delta\delta$ (Hz)

system	$-CH_3$ δ Hz
F68	415.87
Sudan III-F68	405.31
$\Delta\delta$ = {F68: Sudan III-F68} ≈ Sudan III-F68	10.56
IMO-F68	419.71
$\Delta\delta$ = {F68: IMO-F68}	−3.84
Sudan III-IMO-F68	420.12
$\Delta\delta$ = {F68: Sudan III-IMO-F68} ≈ Sudan III-IMO-F68	−4.25

Table 3. Computer Calculations for Systems Carried Out by Means of an Empirical Point Function (Score) and a Coupling Vector (Shape of a Spring) in the ArgusLab Program[X] with a Dock Coupling Protocol (Score/Form) So That All Minimum Energy of Simulated Systems (See Experimentation Methods)[a]

system	component of system 1*	component of system 2*	system or complex ΔG_I (kcal/mol)
Sudan III*-F68*	Sudan III*	F68*	−4.40
IMO*-F68*	IMO*	F68*	−2.81
Sudan III*-IMO*	Sudan III*	IMO*	−2.58
Sudan III*-IMO*-F68*	Sudan III*	IMO*-F68*	−2.79

[a] ΔG_I (kcal/mol) is the calculation corresponding to the energy interactions involved in each of the systems or complexes. The asterisk (*) corresponds to the parts 1* and 2* ("from left to right") of the simulated compounds of the system.

molecules forming the IMO*-F68* and Sudan III*-F68* (Figure 6d) complexes with the corresponding formation energies ΔG_I = −2.81 kcal/mol and ΔG_I = −2.58 kcal/mol, respectively. Finally, ΔG_I = −2.79 kcal/mol was needed to form the Sudan III*-F68*-IMO* (Figure 6c) complex from its components (d) Sudan III*-F68*, (b) IMO*-F68* and (a) Sudan III*-IMO*, respectively.

Raman Spectroscopy of F68. Figure 7a shows the Raman spectra of F68 in the solid state, attributed to the vibration modes of the methylene group ($-CH_2-$) between ∼30 and 70 °C of the cooling cycle (labeled "down") in the corresponding spectra, showing comparatively a sudden change between ∼40 and ∼50 °C. The deconvolutions between 2850 and 2930 cm^{-1} correspond to the symmetric and asymmetric stretching of the methylene group ($-CH_2-$) of the PPO (F68) block. The global analysis of the adjusted parameters (intensity, area, and position) as functions of the temperature of the cooling cycle is represented in Figure 7b. It shows the thermal history of the methylene group at 2930 cm^{-1}. Each curve shows the intensity and area as functions of temperature. Then, it is shown the thermal history of the methylene group at 2930 cm^{-1}. It is seen that both curves are functions of the intensity and area as a function of temperature. This is how three kinds of inflections occur: two consecutive ones at ∼35−40 °C and ∼40−43 °C and one further away at ∼50−58 °C.

Differential Scanning Calorimetry (DSC) of F68. The DSC thermogram of Figure 7b shows two calorimetric flow versus temperature inflections: one at ∼33−40 °C and one at ∼50−58 °C, with a pronounced endothermic peak whose minimum corresponds to ∼56 °C.

High-Resolution Ellipsometry of F68 on SiO_x. In parallel, temperature cycles of 20−80 °C monitored by high-resolution ellipsometry for each F68 film deposited on SiO_x represent the change of the polarization angle (δP) with respect to temperature. This produced graphically the typical

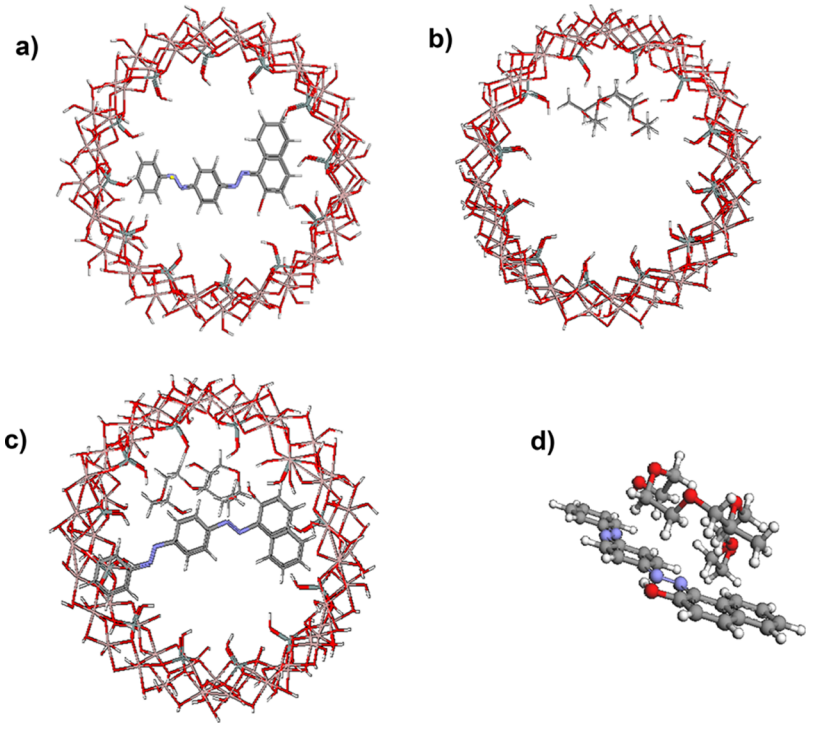

Figure 6. Molecular simulation of (a) Sudan III*-IMO*, (b) IMO*-F68*, (c) Sudan III*-IMO*-F68*, and (d) Sudan III*-F68* (Table 3).

https://dx.doi.org/10.1021/acsomega.9b02965
ACS Omega 2020, 5, 20707−20723

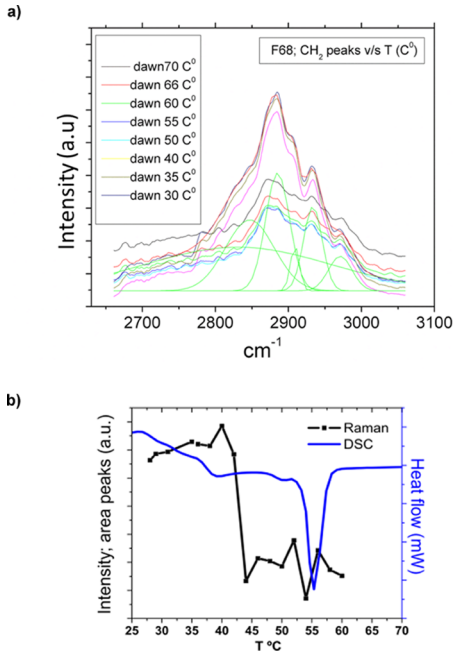

Figure 7. Thermal evolution area of the Raman peaks (around 2850 and 2950 cm^{-1}) (heat rate: 70−30 °C), corresponding to the symmetric an asymmetric stretching of the methylene group ($-CH_2-$) and the DSC calorimetric flow power (mW) of the F68 solid. (a) The Raman peak area change is, around the temperature (black squares), due to the surface transition temperature (low temperature) and bulk transition temperature (high temperature). (b) Likewise, the DSC curve (blue line) shows the falling range corresponding to surface and bulk transitions temperatures.

hills of the superficial melting process of the nanometric films[36] of F68. In Figure 8a, the width of the melting intervals corresponds to the hills formed (δP vs T °C) throughout the increasing thermal cycles. The first two correspond to the concentrations of the (0.5, 2.0) × 10^{-4} M samples and the second to the (6.0, 10.0) × 10^{-4} M concentrations. Figure 8b,c shows two morphological studies referring to the same samples ran in parallel using two AFM microscopes with two different techniques for the samples presented: Figure 8b [0.5 (a), 6.0 (b), 10.0 (d), 20.0 (e)] × 10^{-4} M, (c) ∼height (nm) of the films (drop-casting: AFM contact mode) and Figure 8c [0.5 (a), 6.0 (b), 10.0 (c)] × 10^{-4} M, ∼height of the films (nm) (spin-coating; AFM tapping mode).

Aqueous Phase/1-Octanol Distribution. Figure 9a,b shows the behavior of Sudan III after being transferred from the Sudan III-F68 and Sudan III-IMO-F68 aqueous dispersions to the 1-octanol phase[45,56] as a function of temperature after 48 h (Figure 9a,b). Maximum amounts of Sudan III collected from organic phases were ∼5.0 × 10^{-5} and ∼2.5 × 10^{-5} M, respectively (Figure 9b). Specifically, the aqueous dispersions of Sudan III-F68 and Sudan III-IMO-F68 were at ∼40 and ∼43 °C, respectively. In this way, the maximum of the profile of Sudan III-IMO-F68 was found. It is significant in terms of the ∼3 °C shift. The graph of Figure 9b represents the molar concentration of Sudan III collected in the 1-octanol organic phase[46,57] from the aqueous dispersions of Sudan III-F68 and Sudan III-IMO-F68 (that were between 32 and 50 °C after 48 h) in increasing order for the seven samples of both systems.

DISCUSSION

Characterization and Morphology. The topology of the films observed in the AFM image of Figure 3a,b shows fibers composed of "hollow" nanothreads of imogolite with a minimum height of ∼2.5 nm related to the substrate in Figure 3c, whose longitudinal coverage exceeds 200 nm.[35,58] The formation sequence of the structure of Sudan III-IMO in Figure 4c−f may be due to a set of factors associated with the process of deposition of the hydrogel on the molecules of anhydrous Sudan III. This is dispersed on the substrate in coexistence with evaporation of the drop of hydrogel on anhydrous Sudan III adhered on the substrate in Figure 4a,b. Then, simultaneously, the process of self-assembly of the film would take place in two successive stages: (i) diffusion of the fibers from the liquid that forms the drop toward the cumuli of Sudan III and (ii) once contact has occurred between both. Hydration of molecules of Sudan III takes place, causing them to aggregate in cumuli that are threaded in the "spiderweb" (Sudan III-IMO) due to the spreading of film on the surface of SiO_x.

The peculiar properties and characteristics of the imogolite macromolecule (IMO) make it possible to capture large amounts of neutral molecules of Sudan III.[59] This property has a polarity opposite that of the hydrogel, leading to the formation of compacted packets within the filamentous network. The filamentous is interspersed between the superficial layers (dendrites) of the F68 matrix, finally forming the film of Sudan III-IMO-F68 (Figure 4g−l).

It is quite probable that the fibers intertwined between the Sudan III cores form a very compact lattice of the Sudan III-IMO complex since they are compressed between the upper layers constituted by PPO (block of F68 propylene polyoxide). This flat upper layer is distributed on the upper side of the film shown in Figure 4g−l. The film moves away from the substrate by repulsion since both sides have opposite polarities.

^{1}H-NMR of Systems in Solution. The chemical shift values to aromatic H_1 (Sudan III, see Figure 5b and Table 1), $\Delta\delta$ Hz, of Sudan III-F68, Sudan III-IMO, and Sudan III-IMO-F68 are 13.685, 11.710, 7.620, and 5.910, respectively. The sequence indicates that the interactions of the H_1 hydrogen of Sudan III with the functional groups of F68 and IMO is due to the variability of the main stabilizing forces of the systems that are formed (together with those that belong to the other hydrogens of Sudan III) but which individually are less significant. In general, the shifts to lower fields would be due to competitive types of interactions of H_1 between the components that make up the systems in solution. Specifically, within the ternary system, the H_1−IMO interaction is more favored than H_1−F68 because, in the presence of the IMO component, the H_1−F68 interaction is weakened substantially in favor of significantly shifting to higher fields.

Based on that behavior, an empirical criterion was established associated with each high-field and low-field $\Delta\delta$ Hz of H_1 (Sudan III) (Figure 5a,b and Table 1) and $-CH_3$ (PPO) (Figure 5c and Table 2), respectively. The low-field ones are due to the loss of electronic density, both groups (H_1 (Sudan III) and $-CH_3$ (PPO)) turning more nucleophilic related to each system in solution. Toward high field, the phenomenon is reversed due to their electron gain, which turns them more electrophilic (to each system). The linear correlation between the coordinate set composed of the $\Delta\delta$ Hz of H_1 and the adjustable parameters $\Delta\delta/\sum\Delta\delta$ (also

https://dx.doi.org/10.1021/acsomega.9b02965
ACS Omega 2020, 5, 20707−20723

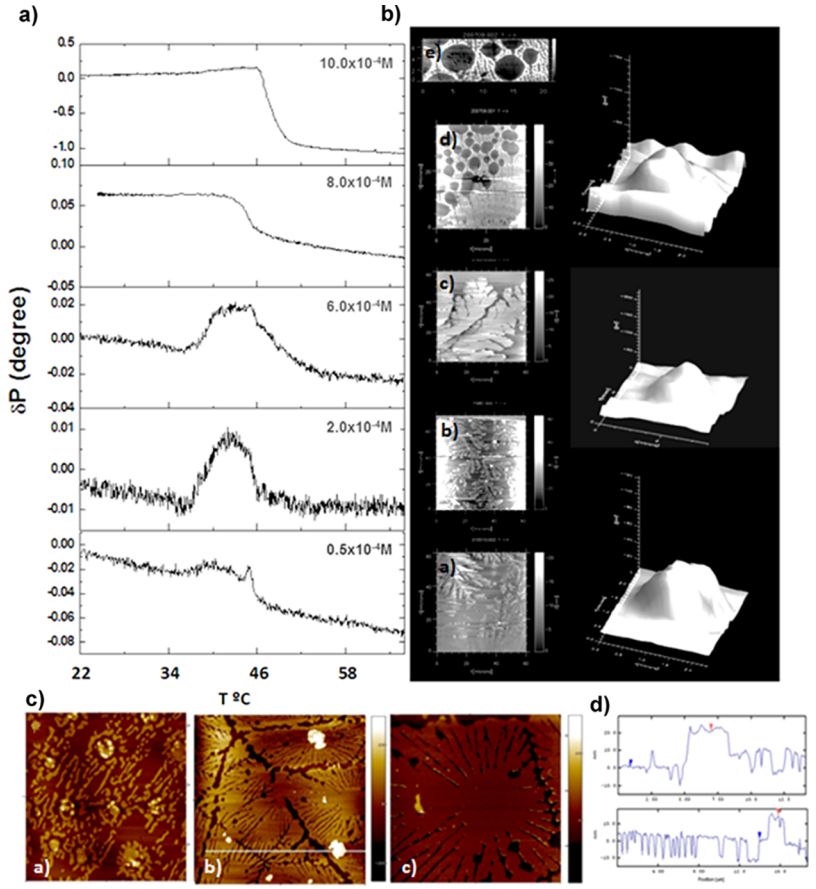

Figure 8. (a) High-resolution ellipsometry determination of films formed to various molar concentrations F68 on SiO_x (drop-casting). The graphs show the changes in d*P* measured for heating ramps of the samples F68. The maxima peaks and inflexion confirm the surface transition temperature of the films. (b) For samples, the sequence of AFM (tipping mode) corresponds (∼middle on figure) to the parallel arrangement (a−d) of the ellipsometries. The images show the general presentative height of the bulk and 2D (film) structure sequences on SiO_x (drop casting), corresponding to a CMC of ∼2.0×10^{-4} M. The top image shows in detail the dendritic web with micrometric size pores (10.0×10^{-4} and 20×10^{-4} M samples). (c) Independently, the AFM (tipping mode) images (bottom of the figure) showing the bulk and dendritic structures of F68 on mica: (a)−(c) ([0.5, 6.0, 10.0] × 10^{-4} M) (spin-coating) with the same average heights.

include the pair of "double peaks"), whose value is the lowest of all the coordinates of Sudan III-F68, Sudan III-IMO, and Sudan III-IMO-F68 in the graph of Figure 10a on the top of that figure. In agreement, the pair of peaks is displaced toward the lowest reference field (5.910 Hz), i.e., to the right of the other values of that correlation. The relative values of 7.620 Hz for H_1 and 5.910 Hz for Sudan III-IMO-F68 show that the Sudan III-IMO complex has the possibility of being distributed in two phases of different polarities within the environment favored by the F68 matrix.[17,18]

On the other hand, the $\Delta\delta$ Hz values of $-CH_3$ (PPO block: F68) at −4.250, −3.840, and 10.560 indicate that, in Sudan III-IMO-F68, IMO-F68, and Sudan III-F68 in the graph of Figure 10 b on the bottom of that figure the group, it loses electronic density to the surroundings in that order. At the same time, the $\Delta\delta$ Hz values of $-CH_3$ and H_1 have low-field values of 10.560 and 13.680 in the Sudan III-F68 system. However, although both groups gain electronic density from the medium, their $\Delta\delta/\sum\Delta\delta$ indices are very different. Compared to the other systems, there is a significant variation toward low fields, hinting that the probability of H_1-CH_3 interaction arises directly.[60] The values of the empirical slopes and indices (nucleophilicity−electrophilicity) of the correlations would be a direct indication that such interactions are predominant factors in the sense that Sudan III-IMO and IMO-F68 components have some stability within Sudan III-IMO-F68 to the detriment of the formation of Sudan III-F68 in the low-field region. This is confirmed by the fact that the H_1-CH_3 interaction of Sudan III-F68 has a rather electrophilic character (to the right) compared to the two nucleophilic characters Sudan III-IMO and IMO-F68 (to the left), always finding IMO in both. On this sight, it is presumed that the H_1-CH_3 interaction competes independently with the H_1−IMO and IMO$-CH_3$ interactions in the ternary system in solution. Therefore, the functional groups follow the trends according to the polarity (higher to lower electrophilicity−nuclophilicity, or vice versa) of the surrounding medium in the order (i) H_1 (Sudan III): Sudan III-IMO-F68 > Sudan III-IMO > Sudan III-F68 and (ii) CH_3(F68): Sudan III-IMO-F68 > IMO-F68 > Sudan III-F68.

The correlations represent a change in the polarity gradient of the chemical groups of the systems in solution. The coordinates of H_1 (Sudan III) and CH_3 (F68) appear in two different polarity planes (high and low fields), above and below the zero value. The composition factors of the correlations ($\Delta\delta$ and $\Delta\delta/\sum\Delta\delta$) follow the lipophilic−hydrophylic behavior of the systems and components in solution. So, although H_1 is in the low-field zone, its trend tends to the limiting value zero in

https://dx.doi.org/10.1021/acsomega.9b02965
ACS Omega 2020, 5, 20707−20723

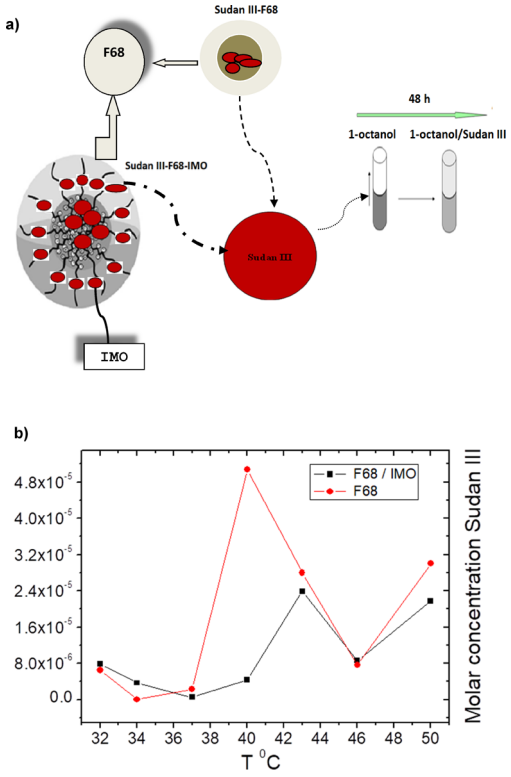

Figure 9. (a) Representative diagram of the distribution of Sudan III from the aqueous phase Sudan III-F68 and Sudan III-IMO-F68 as a function of temperature (32−50 °C) to the corresponding organic phases of 1-octanol in 48 h. (b) Molar concentration of Sudan III (M) collected from each organic phase. The maximum concentration picks coincide with the surface melting temperature (∼38−39 and ∼42−43 °C) of each matrix micelle of F68.

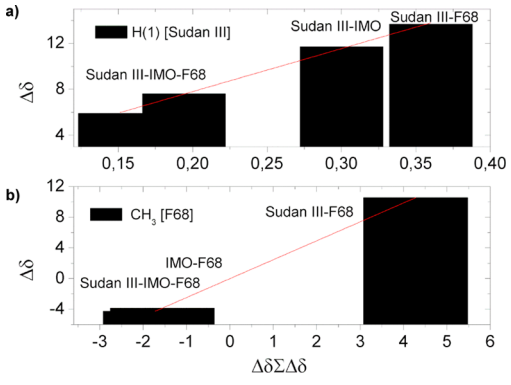

Figure 10. (a) The upper and (b) lower graphs represent ^{1}H-NMR relative spectral shifts based on the linear correlation of the frequency deltas Δ (Hz) versus the "polarity indices" $\Delta\delta/\Sigma\Delta\delta$ [Cartesian coordinates to high field (more lipophilic) and low field (more hydrophilic], both H_1 of Sudan III (Table 1) and that of $-CH_3$ of PPO (F68) (Table 2) of each system indicated in both curves.

the order F68, IMO, and IMO-F68. Therefore, the presence of F68 and IMO in combination with Sudan III generates an increasingly hydrophilic environment that increases the aggregation of the hydrophobe (decrease in the ratio of hydrophobic PPO of the F68 matrix core to hydrophilic PEO of the F68 matrix "mantle"), modifying its nuleophilicity due to the lipophilic−hydrophilic change in favor of a more lipophilic one, i.e., toward zero.[61]

The upper graph belonging to Figure 10a shows the chemical shifts ($\Delta\delta$ Hz) of hydrogen, H_1, of the Sudan III component of the Sudan III-F68, Sudan III-IMO, and Sudan III systems in organic solution (Table 1) as a function of the polarity index, $\Delta\delta/\sum\Delta\delta$, corresponding to each of them. Similarly, the bottom graph in Figure 10b shows the chemical shifts ($\Delta\delta$ Hz) of the methyl, $-CH_3$, of the PPO block of the Pluronic F68 (F68) component of the Sudan III, IMO-F68, and Sudan III-IMO-F68 systems in organic solution (Table 2) as a function of the adjustable polarity index $\Delta\delta/\sum\Delta\delta$, which corresponds to each. Then, the sequence of the AFM images in tapping mode and spin-coating (bottom part of Figure 8b,c) shows the bulk and dendritic structures of the F68 films with approximately the same average height. Likewise, the $-CH_3$ of PPO (F68), which is more hydrophobic,[14] goes from a high-field zone (Sudan III-F68) directly to two lower-field zones very close together (IMO-F68 and Sudan III-IMO-F68). This happens due to incorporation in the same order of IMO and IMO-F68. Thereby, the hydrophilicity of the medium increases around $-CH_3$, increasing the segregation of the PPO block (F68) due to its high hydrophobicity.[62] However, H_1 remains always in the low-field region, as shown by the slope and the nucleophilicity−electrophilicity index $\Delta\delta/\sum\Delta\delta$. The latter is dependent on the intrinsic nature of H_1 and CH_3 according to the polarity gradient provided by phases of components and systems.

Molecular Simulation. The interaction energy ΔG_I = −4.40 kcal/mol in molecular simulation of the Sudan III*-IMO* complex (Figure 6a and Table 3) occurs specifically through hydrogen-bond interactions between the silanol groups (Si−OH) of IMO* ("cross section of imogolite"). The $H_{13\text{-}14\text{-}15}$, H_1, H_2, and H_3 hydrogens of the Sudan III molecule (Figure 5a,b and Table 1) are responsible for the stabilization of the Sudan III* molecule inside the molecular ring (IMO*) (Table 3), as displayed in Figure 6a.

The interaction between the representation of a portion of F68 with the methyl group of PPO of interacting with another portion of IMO was discussed (Figure 5c and Table 2). It is represented by the simplified model F68*: $[(EO)_2\text{-}(PO)\text{-}(EO)_2]$. Then, the F68*-IMO* dimer as shown in Figure 6b and the Sudan III* molecule give rise to the IMO*-F68* and Sudan III-F68* as shown in Figure 6c: complexes with energy differences ΔG_I = −2.81 kcal/mol and ΔG_I = −2.58 kcal/mol, respectively (Table 3). The simulations show that two blocks of F68* $\{[EO)_2\text{-}(PO)\}$ interact with three silanol (Si−OH) groups of the (IMO*) molecular ring, leaving the end of the $[EO]_2$ dimers outside of the ring. Thus, Sudan III*-F68* as shown in Figure 6d is slightly more stabilized than the former, not showing direct interactions between the functional groups belonging to the Sudan III* and F68* components (Table 3). However, Sudan III*-IMO*-F68* (Figure 6c and Table 3) has almost the same stability as IMO*-F68*. Thus, the interaction with component F68* appears to be the apparent cause for the ternary system (Sudan III*-IMO*-F68*) to be less stabilized with respect to Sudan III*-IMO*. This would occur because the Sudan III* component is found inside together with the segment of the $\{[EO]_2\text{-}[PO]\text{-}\}$ block, and the other portion of the $[EO]_2$ block is outside the IMO* ring.

Relation between ^{1}H-NMR, Morphology, and Simulation. The greatest chemical shifts occur through the hydrogens of Sudan III, which are involved in the systems that contain IMO and F68. Particularly, in the case of H_1 (Table 1), those interactions are rather slight, occurring more

https://dx.doi.org/10.1021/acsomega.9b02965
ACS Omega 2020, 5, 20707−20723

probably near the proton. For that reason, in a ternary system, a smaller chemical shift would be due mainly to the presence of the IMO component weakening the interaction with the F68 matrix because of competitiveness between both components.

These F68 slides occur more frequently (dendritic sheets aggregates), where large numbers of the articular zone forming cavities converge ("nodal distribution formed by the pores of ∼1.5−2.0 nm in the fibrous network of the IMO": Figures 1 and 3a,b). Such molecular contacts guide the capture of Sudan III (Figures 9a, 6c,d, and 4a−f). Most remain outside, being distributed through deployed nanofibers together with Sudan III aggregates (Figure 4g−l). The fibers become tensed as aggregates move away from the nucleus as they approach the hydrophilic layer (Figure 4c,d). Impulse force, promoted by polarization changes in Figure 10a,b, is induced by the hydrophobic nature of H_1 (Sudan III) and CH_3 (F68) in Sudan III-F68, Sudan III-IMO, and Sudan III-IMO-F68, respectively.

It is also suggested that Sudan III, F68, and Sudan III-IMO components suffer high-field shifts in Sudan III-IMO-F68 (Figure 10a,b), given that correlative intensifications of H_1 (Sudan III) and CH_3 (F68) interactions in Sudan III-IMO-F68 are based on "polarity indexes". According to our information, it is possible that H_1−OH−Si and CH_3−OH are generated into the nanotubular pore (molecular ring IMO represented in Figure 6a−c). From here, platform (flats) forming structures (Figure 6d) that extend to the outskirts of Sudan III-F68 are conformed, forming condensed and interconnected regions of similar polarity, allowing the coexistence of continuous interfaces within the micelles (Figure 9a)).

According to the above, such interactions intensify their activity even more since core layers compact the nucleus increasing system hydrophobicity. Lipophillicity increases the closer a microenvironment is to its center, and inversely, it decreases. Thus, the confined space that contains them becomes narrower[63] in Sudan III-IMO-F68 as the PPO ($-CH_3$) [F68] and Sudan III (H_1) share their aggregated parts. The anchorage of PPO to IMO according to inferences occurs via intramolecular $-CH_3-CH_3-$ and intermolecular H_1-CH_3 interactions, generated mainly in nodal regions rather than on extended nanothreads. However, both depend on the stability of Sudan III-IMO intercalated between reticular dendrites (F68), which geometrically covers the formed complex (Figure 4g−l).

The double signal in H_1 spectra ("double peaks") to the right in Figure 5b (black polygon) plays an important role in the compatibility of Sudan III. The concept of polarization indicates that the micelles maintain at least two concentric phases. Therefore, the more lipophilic phases retract toward the micellar center, decreasing their influence in the opposite direction. Sudan III-F68 (Figure 9a) spectra suggest that interactions between H_1 (Sudan III) and CH_3 (PPO [F68]) (Figure 5a−c) become weaker since there is no Sudan III-IMO with specific joint sites (Figure 1). However, H_1-CH_3 and H_1−Si interactions in Sudan III-F68 provide stability by increasing the confinement in Sudan III-IMO-F68. Such bindings contribute to repulsion of liposolubilized layers. This repulsion extends hydrophilic layers that compress the central and peripheral hydrophobic regions of the core until segregation occurs from the hydrophilic phase of the micellar shell. Analyzing more in technical detail, the mechanisms from these phenomena were complemented the theoretical information of computational dynamic systems.

Thus, that interaction is lost completely in the IMO-F68 and Sudan III-IMO-F68 systems, where the displacement of the methyl group (PPO of the F68 matrix) is oriented to high field, caused by the loss of electron density toward IMO more than toward H_1, compared to Sudan III-F68 (Tables 2 and 1). So, in Table 1, the H_4 and $H_{11\text{-}15}$ hydrogens of Sudan III show a similar chemical shift to high field, therefore assuming the existence of other contributions to the general stability of Sudan III-IMO. However, the simulation of Figure 6a shows that H_4 (Figure 5a and Table 1) is farther away than hydrogens H_1, H_2, and H_3 (Figure 5a and Table 1) in the molecule of Sudan III* with respect to the OH groups of the IMO* ring. Also, hydrogens $H_{11\text{-}15}$ (Figure 5a and Table 1) of Sudan III* (Table 3) are even further away than hydrogens $H_{13\text{-}14\text{-}15}$ (Figure 5a and Table 1), not showing a direct interaction explicitly. Nevertheless, in the simulation, those hydrogens are no more than ∼5 Å from the Si−OH groups (IMO*), and they may be hypothetically involved in "intermittent" or partial interactions that would contribute to the general stabilization of the real systems in solution.

It can be assumed that the analyzed chemical shifts are caused by interactions between the hydrogens of Sudan III and the silanol groups inside the openings of IMO. In this way, the latter form a set that would be inserted along the nanofibers, allowing the formation of the "spiderweb" by the Sudan III-IMO complex (explaining the simulation Sudan III*-IMO* complex). Complementarily, the molecular simulation together with the ^{1}H-NMR analyses confirm the probability that the interaction between H_1 (Sudan III) will take place mainly in the Si−OH group (IMO) in two separate ways. It is manifested by two hydrophilicities−hydrophobicities due to two different polarities within Sudan III-IMO-F68. The high and low fields of the methyl group F68 in systems Sudan III-F68 and Sudan III-IMO-F68 (^{1}H-NMR) agree with Sudan III*-F68* and Sudan III*-IMO*-F68* simulated complexes. According to experimental evidence, the methyl group CH_3 (F68*) would interact directly with the hydrogens of Sudan III* (H_1). However, the methyl group F68* would not be so favored with respect to interaction between the IMO* group (Table 3) as is shown analogously in ^{1}H-NMR.

The simulation approaches the experimental interpretation (Tables 1 and Table 2) in the sense that it reveals a rather slight interaction in Sudan III*-F68* (Table 3 and Figure 6d).

Based on these assumptions, a section of Sudan III-F68 would remain inside the internal diameter pore of ∼ 1.5−2.0 nm of the IMO nanotube (Figure 1) and the other part of the hydrophilic block $[EO]_2$ of F68 outside the pore (around their outside: Figure 6c) interacting with the nanotubes (Figure 4a−l). This implies that, when IMO is present, the formation of the Sudan III-IMO complex is favored to the detriment of Sudan III-F68. In this way, the complex inside the ternary system has the possibility of being in two phases with different polarities (hydrophobic and hydrophilic) provided by the F68 matrix.

On the other hand, according to the morphological study, the upper part of the laminar dendrite surface of F68, where the lipophylic part of PPO is mainly found, has affinity for specific parts of the Sudan III-IMO network threading itself. Furthermore, the complex is substantially immersed in the phase composed of PEO (F68) blocks, possibly due to the exposure of the Al−OH groups (IMO) to the hydrophlic phase of F68. However, it was not possible to get the ^{1}H-NMR

https://dx.doi.org/10.1021/acsomega.9b02965
ACS Omega 2020, 5, 20707−20723

of the functional groups of IMO because they are hidden by the wide OH band of the water in the systems.

The main causes for the complex to be distributed in the lipophilic and hydrophilic phases are interactions that keep the Sudan III-IMO complex stabilized. Thereby, $H_1-Si-OH$ interaction remains important compared to interaction H_1-CH_3, the one that keeps Sudan III-F68 stabilized. In the self-assembly of the ternary system Sudan III-IMO-F68 in solution, the stable diffusion of complex Sudan III-IMO (mobile phase) toward the phases of F68 takes place because the latter has lower competitive interactions with the matrix (H_1-CH_3: Sudan III-F68 and PEO-Al-OH: IMO-F68). Both interactions between H_1-CH_3 and IMO-F68 have sufficient affinity for both components to remain compatibilized. In short, compatibility of the complex and matrix is generated by factors of a lipophilic and hydrophilic character present in Sudan III-IMO and F68 inside Sudan III-IMO-F68 in solution.

For the relation between Raman, DSC, and ellipsometry-AFM, the inflections of the Raman spectra curves coincide with the inflections seen in the DSC thermogram (Figure 7b). The melting of the F68 bulk material marked by the minimum value of the endothermic peak (DSC) at ∼56 °C is in the range of both inflections of the Raman spectra, where the minimum is ∼54 °C. On the other hand, the inflections of the Raman spectra between ∼35 and ∼40 °C fall within the range of ∼33−40 °C of the first inflection of the DSC thermogram.

Similarly, the second inflections between ∼40 and ∼43 °C of the Raman spectra agree with the intervals of the superficial melting process of the F68 films on SiO_x, between ∼39 and ∼44 °C, obtained by high-resolution ellipsometry, showing the sequence of δP vs T (Figure 8a) (films formed from the F68 aqueous solution aliquots, with different molar concentrations).

The intermediate stage of the Raman spectra, which goes from ∼43 to 50 °C, also agrees with the other consecutive ellipsometric interval of ∼44−50 °C. Both consecutive stages of the superficial melting process (∼39−44 °C and ∼44−50 °C) depended on the lower concentrations of F68 deposited on SiO_x (set, [0.5 and 2.0] × 10^{-4} M of F68). The two hills, which bound the superficial melting intervals (low concentrations), would indicate two consecutive melting processes of the films. However, the one corresponding to the 6.0 × 10^{-4} M (F68) concentration shows practically only one well-defined hill, but the typological reminiscences of the two hills that bound the two consecutive melting stages by the lower concentrations deposited on the substrate are still present. In the substrates on which the 8.0 × 10^{-4} and 10.0 × 10^{-4} M concentrations were deposited, melting intervals turn increasingly more like a "bulk" melting process. This process located in the intermediate zone that bounds superficial and "bulk" melting processes are attributed to F68 solid in the Raman and DSC graphs (Figure 7b).

At the same time, the morphological experiments carried out by AFM revealed that the films on Figure 8b depend on the amount of (F68) material deposited on the SiO_x. This shows that density of dendrites increases together with the coverage of surface area of the substrate as a function of molar concentration of samples. The altitude of films remains practically invariable along the cross section of sheets, ∼10−20 nm, and not exceeding ∼25 nm on Figure 8b,c. According to these results, the "bulk" material structures of the films undergo a thermodynamic transition, turning into the 2D "bulk" structures when the concentration is greater than ∼0.5 × 10^{-4} M. Thus, dendritic coverage increases significantly above the critical micelle concentration (CMC) of F68[15] (CMC and its correlation with morphology versus the increase cell viability of human neuronal model in vitro; corroborates carrying capacity Sudan III into F68 micelles in aqueous medium and human plasma).

The phenomenon (cell viability of human neuronal model[15]) is seen even until the film becomes saturated by excessive dendrites at 20.0 × 10^{-4} and 10.0 x 10^{-4} M (on the top of Figure 8b), respectively. Consequently, the inflections of the Raman curves (Figure 7a,b) between ∼39−43 and ∼43−50 °C correspond to a superficial melting process, characteristic of the laminar phases of F68. In a concentration of 20.0 × 10^{-4} M, no measurements were obtained in Figure 8a to analyze them morphologically by AFM on the top of Figure 8b. In this regard, this should be due to saturation with the porous layers that cover substratres. This causes that, together, the assembled structures of the films approach progressively the characteristics of F68 "bulk" material, as it happens with the 8.0 × 10^{-4} and 10.0 × 10^{-4} M samples, respectively.

Both empirically and experimentally, the release of Sudan III in the Sudan III-F68 and Sudan III-IMO-F68 systems is demonstrated by the amount of Sudan released to organic hydrophobic phase 1-octanol in Figure 9a,b. The thermal and morphological analysis (Raman, DSC, and AFM-ellipsometry) in Figures 7a,b and 8a−c shows that release depends largely on thermal properties of the F68 component in both systems in aqueous solution.

The curve in Figure 9b represents the maximum concentration of Sudan III released by Sudan III-F68 at ∼40 °C (5.0 × 10^{-5} M). This agrees with the melting attributed to the superficial layers of F68 (Figures 7b and 8c) that are represented in the AFM images (Figure 8b). The last image shows in detail that the dendritic web is pierced by micrometric pores[64] that go through the layers perpendicularly, from the upper ones of PPO to the lower ones of PEO that are on SiO_x.

The studies show that the superficial melting comprises the hydrophilic shell (PEO) and the hydrophobic core (PPO) of F68 in the solution systems.[62] So, at the superficial melting point, the superficial layers of the F68 micelle are dilated significantly, releasing the maximum amounts of the contained hydrophobe to the lipophilic medium. Similarly, the profile of the Sudan III-IMO-F68 curve indicates that the maximum amount of Sudan III released, which is 2.5 × 10^{-5} M at ∼43 °C, follows the melting pattern of the superficial layers of F68, but out-of-phase by ∼3 °C (Figure 8a)). Specifically, high retention capacity would be a cause of great stability of the Sudan III-IMO complex compatibilized with F68, forming Sudan III-IMO-F68. The drastic polarity changes of the latter compared to Sudan III-F68 confirms such a property (Figure 10a,b).

The thermal behavior of micelles of F68 is due to a superficial melting process. Thus, the superficial melting intervals of the "bulk" material determined by Raman and ellipsometry of the F68 films agree with the profile of the hydrophobe released by Sudan III-F68 at ∼40 °C. On the other hand, the maximum amount released (2.5 × 10^{-5} M) by the tertiary system Sudan III-IMO-F68 system at ∼43 °C corresponds to one-half amount released by the binary system Sudan III-F68 system. Therefore, The Sudan III-IMO-F68 of ∼3 °C compared Sudan III-F68 system, is due to stability of complex Sudan III-IMO compatible with the F68 matrix. The

https://dx.doi.org/10.1021/acsomega.9b02965
ACS Omega 2020, 5, 20707−20723

thermodynamics following the morphological change of films as a function of concentration of each F68 dispersion recreates coherently the physicochemical functioning of F68 micelles in the aqueous phase above the CMC. Furthermore, retention of hydrophobe by Sudan III-IMO-F68, compared to Sudan III-F68 (~43 and ~40 °C in Figure 9b), is evidenced by the large polarity difference (Figure 10a,b). So, the Sudan III-IMO-F68 system is further intensified of the H_1-CH_3 interaction compared to the Sudan III-F68 system.

Acccording results maximum retaining capacity of hydrophobic molecules it due to the Sudan III-IMO complex inside the F68 matrix.[35,38,65−67] In the experimental (Figure 9), Sudan III by the Sudan III-IMO-F68 device is doubled at ~43 °C compared to the classic Sudan III-F68 system at ~40 °C. This was attributed to mutual affinity between the Sudan III-IMO complex and F68 matrix as a result of the compatibility among both components since it forms compound micelles. In this way, the device becomes a lipophilic drug delivery model in vitro delays the release of "drug" (Sudan III), for example, under conditions that are considered "pathological" as for temperature human body.[27,68,69]

Nevertheless, the CMC of Sudan III-F68 with respect to morphology of the F68 matrix (F68 film covering the substrate SiO_x), surface tension, and cell viability have significant changes that are consistent with modification and penetration capacity into the plasma membrane.[15] On the other hand, the CMC of Sudan III-IMO-F68 was unmodified because solitary IMO strands attached to Sudan III formed Sudan III-IMO into the F68 matrix. The Sudan III-IMO-F68 composite applied for the prolonged release for selective hydrophobic drug administration compatibilized with imogolite hydrogel. The material Sudan III-IMO-F68 is more hydrophobic than Sudan III-F68 and carried out prolonged release Sudan III ("drug") captured by the water−octanol interface phase at a determined temperature.

The results of evaluation are congruent with observations of F68 morphological and physicochemical properties, showing the ability to trap and release hydrophobic "drugs" in a controlled manner. This does increases the ability to trap and release "lipophilic medicament" without variations in the CMC.[15] Everything by control of imogolite interactions with Sudan III particles in the fractal morphology matrix is a function of temperature. Sudan III-IMO is formed on a hydrophilic surface mainly determined by IMO gel hydrations in the precursor solution of films. Thus, the complex (Sudan III-IMO) determines the surface properties of "super-micelles" Sudan III-IMO-F68. Then, transports prolong releasing a maximum amount under surface control of polarization of the matrix sensitive in temperature in "physiological medium under anomalous conditions". Therefore that it are feasible the drug transporters (micelles Sudan III-IMO-F68) specifically target to the damaged organs.

The new hybrid material Sudan III-IMO-F68 not reported with additional qualities too is due to the properties that pertain to imogolite fibers (besides properties F68). This "friendly" new material has advantages and qualities, being to delay release significantly of lipophilic drugs into the objective at determined temperatures. Due to that, this new material could be a powerful restorer of the damaged tissue (tissue engineering and other related applications), given the properties and qualities studied in this work.

Finally, the evaluation of the physical−chemical phenomena and the characterization of copatibilized components that form a new system of material designed maximizes loading and delivery capacity of a lipophilic drug at the objective site. Therefore, the micellar microdevice extends the controlled release of the "drug" to the target or physiological medium. This is essentially for selective administration of hydrophobic anti-inflammatories directed toward the central nervous system or other organs of the body for therapeutic purposes.

Therefore, due to characteristics and properties acquired by the new designed material, we are about to verify experimental application of Pluronic F68 compatible with imogolite in corresponding proportion. Then, we hope that, in addition to improving the effect of medication, it will increase regeneration of the damaged tissue at the specific site previously determined.

Rational Retrospective. Sudan III-IMO-F68 obeys the thermodynamic reversibility of F68 and the CMC that does not vary, even though Sudan III-IMO into F68 is encapsulated. This is evidenced by spectral shifts representing polarization associated with retracted hydrophobic faces without "contact" with the hydrophilic faces segregated more extended inside the composite micelle considered. So in this way, such a device (Sudan III-IMO-F68) is able to release the maximum amount corresponding to the "peak" of F68 at ~42−43 °C in 48 h (Figure 9). Everything in relation to fusion "peak" of F68 at ~37−40 °C (with a shift ~4 °C) through incorporation of IMO fibers slows delivery by Sudan III-IMO-F68 compared to Sudan III-F68. The larger area fusion "peak" (films) coincides with a CMC of $\sim 2.0 \times 10^{-4}$ M (F68), and above 8.0×10^{-4} M (F68), the films fuse as solid F68 (Figure 8).

Projected hydrophobic platforms (or flat) from center to shell, guided by the polarization of H_1 (Sudan III) and CH_3 (F68), are criteria for affinity between Sudan III-IMO and F68. Stability of Sudan III-IMO-F68 shown by the double signal in the energy high field (^{1}H-NMR: Figure 5c) indicates the existence of concentric layers, whose hydrophobic core domains are surrounded by lower hydrophobic phases. Intramicelles, Sudan III-IMO and IMO-F68, increase hydrophobicity more than micelles Sudan III-F68 as opposite polarity packaging-unfolding causes EO blocks to unravel by "above" stretching hydrophilic phases. While PPO blocks circumambulate together with the Sudan III-IMO clusters attached to "solitary" strands, which tense as they unravel and move away from each other. The double signal shows evidence that Sudan III-IMO-F68 is more hydrophobic than Sudan III-F68 (Figure 5c).

"Independent" interfaces widen their separations continuously increasing the ejection of "drugs" by micropores that open in matrix F68, slowly releasing the maximum amount corresponding to endothermic surface fusion "picks" at ~45−47 °C. This reveals that the larger area coincides to a CMC of $\sim 2.0 \times 10^{-4}$ M (matrix F68). Thus, above 10.0×10^{-4} at ~48 °C, supra-structural cohesion gives way to matrix-type "bulk" fusions. Finally, at ~42.5 °C (dephased ~3.5 °C from ~40 °C for surface matrix F68), it indicates that the Sudan III-IMO-F68 device would maintain lower release and biodistribution over time than the Sudan III-F68 device.

Application. The frequency with which pluronic primers ("unimers") interact with Pgp receptors.[70,71] This controls the flow of drug entry into the cells, depend on the amount of "unimer"-Pgp complex formed on the outside of the plasma membrane of these cells, for example, ostensibly improving preferential accumulation in rat brains.[72] This causes the ability to seal the membranes increases cell viability.[16] In addition to

https://dx.doi.org/10.1021/acsomega.9b02965
ACS Omega 2020, 5, 20707−20723

considering this effect, the new prototype can increase drug release by increasing the physiological temperature.[28,35]

Observed through ultrasound, the unimer movement modes (F68) coordinate receptors by enhancing preferential accumulation of an antitumor in the injured rat carotid artery by a tumor.[73] Likewise, vascular permeability increases cytotoxicity of endothelial cells of bovine aorta damaged at a temperature of ∼42.5 °C, which improves preferential accumulation of the micelles loaded with the drug within such cells. This adds to the effect produced by the "free" EO (unimers) that "impacts" couple and decouple P-gp, producing fluidization of the bovine aorta endothelium.[74,75] In skin wounds, temperatures reach ∼45 °C or higher,[76] same as local heat, which releases the maximum content.

In this context, the regenerative effect of the new material would have to be tested experimentally since it is compatible with Pluronic F68-imogolite. Thus, the device has power to be a drug and/or other active release under temperature conditions. The effectiveness of this new prototype is expected to have advantages over other commercial products, for example, compared to QuikClot. For the device composed (QuikClot) of a kaolin-based gauze (aluminosilicate of chemical formula $Al_2SiO_5(OH)_4$ impregnated in a nonwoven polyester-rayon gauze), it has power to accelerate the healing process of serious wounds. Among other things, this is due to an increase in temperature (44.6 ± 1.0 °C) at the wound site. From this perspective, this work also has potential applications to the field of regeneration damaged tissue (tissue engineering).

Hydrophilic shell-IMO with more power vibrational (major rigidity of the chain due hydrophilic PEO) allows it to get have much unimerics on membranous surfaces. This results in a greater fluidization and retention by target cells according to the polarization and equilibrium $\Delta G^0 \approx RT \ln[\mathrm{CMC}]$ (G^0 and R are the Gibbs standard free energy and universal constant of gases[35]). This is due to the number of contacts with the P-gp receptors[71] and it is energetically similar that it form the complexes "unimeric"-P-gp (kinetic phenomenon[77]). These kinetic mechanisms activate specific input−output (drug carrier-hydrophobics). This activates the fluidification that trigger therapeutic effects. Thus, anti-depressants or anti-inflammatories sent directly to the brain could reverse inflammation and apoptosis of neurons[26] or other demage tissues,[17,18,78−83] even with more power depending on body temperature.

CONCLUSIONS

The Sudan III-IMO-F68 system was studied centered on the parts and specific interactions in the solid state and solution. AFM morphological analysis, together with results of ^{1}H-NMR and molecular simulation, agreed univocally that the "spider-web" architecture of the Sudan III-IMO complex is the main cause for the ternary system Sudan III-IMO-F68 to retain a large amount of Sudan III compared to the binary system Sudan III-F68. The molecules of Sudan III aggregated as cumuli are alone, and they are always together with the IMO nanofibers. This is because, inside the nanotube openings (mouths), the Si−OH groups have great affinity for the surrounding hydrophobe. Therefore, a section of Sudan III cumulus is implanted in the mouth (internal diameter pore, ∼1.5−2.0 nm), leaving the cores of the hydrophobe anchored into imogolite network, with a large portion remaining on outside of pores, as shown by morphological analysis AFM on the mica substrate (tapping mode).

Self-assembly of Sudan III-IMO-F68 in solution generates micelles, leaving diffusing the Sudan III-IMO between the concentric layers of F68 (formed by PPO and PEO surrounded by water). In this way, retention of the Sudan III (hydrophobe) by the Sudan III-IMO-F68 system is greater compared to the Sudan III-F68 system. It is seen in the release to phase 1-octanol phase as a function of temperature, in agreement with the drastic change in polarity toward high field in ^{1}H-NMR. So, the maximum amounts Sudan III released in a 2:1 proportion by Sudan III-F68 at ∼40 °C and Sudan III-IMO-F68 at ∼43 °C correspond to the macromolecular behavior above the CMC (F68), together with superficial melting layers of the micelles F68. This is shown by the thermal-morphological analysis made by ellipsometry (in a function of temperature) and AFM (contact mode) of F68 films on SiO_x, which were formed from aqueous solutions as a function of concentration and temperature. In conclusion, the superficial melting of the F68 matrix of Sudan III-IMO-F68 is manifested by the retarded release of the "drug" at ∼43 °C due to compatibilization of components Sudan III-IMO and F68 compared with Sudan III-F68 to ∼40 °C. Thus, a new material constituting Sudan III-IMO-F68, the extended release device, operates optimally under temperature physiological conditions considered "pathological".

AUTHOR INFORMATION

Corresponding Author

Vicente D. Samith − *Departamento de Química, Facultad de Ciencias, Universidad de Chile, Santiago 244355, Chile; Institute for Medical and Biological Engineering, Schools of Engineering, Biological Sciences and Medicine, Pontificia Universidad Católica de Chile, Santiago 7800003, Chile;* orcid.org/0000-0003-0945-3965; Email: vdsamith@uc.cl

Authors

Sebastián Navarro − *Departamento de Química, Facultad de Ciencias, Universidad de Chile, Santiago 244355, Chile*

Reza Dabirian − *Departamento de Quimica, Facultad de Ciencias, Universidad de Chile, Santiago 244355, Chile; Istituto per la Sintesi Organica e la Fotoreattività, Consiglio Nazionale delle Ricerche, 40129 Bologna, Italy*

Complete contact information is available at: https://pubs.acs.org/10.1021/acsomega.9b02965

Notes

The authors declare no competing financial interest.

ACKNOWLEDGMENTS

This work was supported by the always "mythical" University of Chile ("La Casa de Bello"), the Millennium Basal Financing Program (CONICYT), FB0807 (CEDENNA: Line 5, Professor Guillermo González M) and Inorganic Synthesis and Electrochemical Laboratory of Faculty of Science, University of Chile. The authors thank funds from VID, University of Chile and Independent Research Metal-Nano-biotica, Vicente Daniel Samith Monsalve (rut: 9.668.059-7), both for their personal and intellectual monetary contributions that were the majority in this work.

https://dx.doi.org/10.1021/acsomega.9b02965
ACS Omega 2020, 5, 20707−20723

REFERENCES

(1) Chen, C.; Zhou, J. L.; Han, X.; Song, F.; Wang, X. L.; Wang, Y. Z. A Prodrug Strategy Based on Chitosan for Efficient Intracellular Anticancer Drug Delivery. *Nanotechnology* **2014**, *25*, 255101.

(2) Chelushkin, P. S.; Lysenko, E. A.; Bronich, T. K.; Eisenberg, A.; Kabanov, V. A.; Kabanov, A. V. Polyion Complex Nanomaterials from Block Polyelectrolyte Micelles and Linear Polyelectrolytes of Opposite Charge. 2. Dynamic Properties. *J. Phys. Chem. B* **2008**, *112*, 7732−7738.

(3) Kim, B. Y. S.; Rutka, J. T.; Chan, W. C. W. Nanomedicine. *N. Engl. J. Med.* **2010**, *363*, 2434−2443.

(4) Kabanov, V. A.; Skobeleva, V. B.; Rogacheva, V. B.; Zezin, A. B. Sorption of Proteins by Slightly Cross-Linked Polyelectrolyte Hydrogels: Kinetics and Mechanism. *J. Phys. Chem. B* **2004**, *108*, 1485−1490.

(5) Massaro, M.; Colletti, C.; Lazzara, G.; Riela, S. The Use of Some Clay Minerals as Natural Resources for Drug Carrier Applications. *J. Funct. Biomater.* **2018**, *9*, 58.

(6) Bonini, M.; Gabbani, A.; del Buffa, S.; Ridi, F.; Baglioni, P.; Bordes, R.; Holmberg, K. Adsorption of Amino Acids and Glutamic Acid-Based Surfactans on Imogolite Clays. *Langmuir* **2017**, *33*, 2411−2419.

(7) Yamamoto, K.; Otsuka, H.; Wada, S.-I.; Sohn, D.; Takahara, A. Transparent Polymer Nanohybryd Prepared by in Situ Syntresis of Aluminosilicate Nanofibers in Poly(Vinyl Alcohol) Solution. *Soft Matter* **2005**, *1*, 372−377.

(8) Tani, M.; Liu, C.; Huang, P. M. Atomic Force Microscopy of Synthetic Imogolite. *Geoderma* **2004**, *118*, 209−220.

(9) Jiravanichanun, N.; Yamamoto, K.; Kato, K.; Kim, J.; Horiuchi, S.; Yah, W.-O.; Otsuka, H.; Takahara, A. Preparation and Characterization of Imogolite/DNA Hybrid Hydrogels. *Biomacromolecules* **2012**, *13*, 276−281.

(10) Yamamoto, K.; Otsuka, H.; Takahara, A.; Wada, S. I. Preparation of a Novel (Polymer/inorganic Nanofiber) Composite through Surface Modification of Natural Aluminosilicate Nanofiber. *J. Adhes.* **2002**, *78*, 591−602.

(11) Barrett, S. M.; Budd, P. M.; Price, C. The Synthesis and Characterization of Imogolite. *Eur. Polym.J.* **1991**, *27*, 609−612.

(12) Nakano, A.; Teramoto, N.; Chen, G.; Miura, Y.; Shibata, M. Preparation and Characterization of Complex Gel of Type I Collagen and Aluminosilatae Cointaining Imogolite Nanofibers. *J. Appl. Polym. Sci.* **2010**, *118*, 1867−2488.

(13) Jiravanichanun, N.; Yamamoto, K.; Irie, A.; Otsuka, H.; Takahara, A. Preparation of Hybrid Films of Aluminosilicate Nanofiber and Conjugated Polymer. *Synth. Met.* **2009**, *159*, 885−888.

(14) Kozlov, M. Y.; Melik-Nubarov, N. S.; Batrakova, E. V.; Kabanov, A. V. Relationship between Pluronic Block Copolymer Structure, Critical Micellization Concentration and Partitioning Coefficients of Low Molecular Mass Solutes. *Macromolecules* **2000**, *33*, 3305−3313.

(15) Samith, V. D.; Miño, G.; Ramos-Moore, E.; Arancibia-Miranda, N. Effects of Pluronic F68 Micellization on the Viability of Neuronal Cells in Culture. *J. Appl. Polym. Sci.* **2013**, *130*, 2159−2164.

(16) Serbest, G.; Horwitz, J.; Barbee, K. The Effect of Poloxamer-188 on Neuronal Cell Recovery from Mechanical Injury. *J. Neurotrauma* **2005**, *22*, 119−132.

(17) Aydin, F.; Chu, X.; Uppaladadium, G.; Devore, D.; Goyal, R.; Murthy, N. S.; Zhang, Z.; Kohn, J.; Dutt, M. Self-Assembly and Critical Aggregation Concentration Measurements of ABA Triblock Copolymers with Varying B Block Types: Model Development, Prediction, and Validation. *J. Phys. Chem. B* **2016**, *120*, 3666−3676.

(18) Zhang, Y.; Li, Q.; Welsh, W. J.; Moghe, P. V.; Uhrich, K. E. Micellar and Structural Stability of Nanoscale Amphiphilic Polymers: Implications for Anti-Atherosclerotic Bioactivity. *Biomaterials* **2016**, *84*, 230−240.

(19) Sosnik, A. Drug Self-Assembly: A Phenomenon at the Nanometer Scale with Major Impact in the Structure-Biological Properties Relationship and the Treatment of Disease. *Prog. Mater. Sci.* **2016**, *82*, 39−82.

(20) Angelini, G.; Gasbarri, C.; Kazarian, S. G. Pluronic L121, BMIM BF4 and PEG-400 Comparision to Identify the Best Solvent for CO_2 Sorption. *J. Mol. Liq.* **2018**, *258*, 85−88.

(21) Abdul Rub, M.; Azum, N.; Asiri, A. M. Binary Mixtures of Sodium Salt of Ibuprofen and Selected Bile Salts: Interface, Micellar, Thermodynamic, and Spectrosscopy Study. *J. Chem. Eng. Data* **2017**, *62*, 3216−3228.

(22) Kumar, D.; Hidayathulla, S.; Rub, M. A. Association Behavior of Mixed System of the Antidepressant Drug Imipramine Hydrochloride and Diotyl Sulfosuccinate Sodium Salt: Effect of Temperature and Salt. *J. Mol. Liq.* **2018**, *271*, 254−264.

(23) Nishiyama, N.; Kataoka, K. Nanostuctured Devices Based on Block Copolymer Assemblies for Drug Delivery: Designing Stuctures for Enhanced Drug Function. *Adv. Polym. Sci.* **2006**, *193*, 67−101.

(24) Maskarinec, S. A.; Hannig, J.; Lee, R. C.; Lee, K. Y. C. Direct Observation of Poloxamer 188 Insertion into Lipid Monolayers. *Biophys. J.* **2002**, *82*, 1453−1459.

(25) Lee, R. C.; River, L. P.; Pan, F. S.; Ji, L.; Wollmann, R. L. Surfactant-Induced Sealing of Electropermeabilized Skeletal Muscle Membranes in Vivo. *Proc. Natl. Acad. Sci. U. S. A.* **1992**, *89*, 4524−4528.

(26) Curry, D. J.; Wright, D. A.; Lee, R. C.; Kang, U. J.; Frim, D. M. Surfactant Poloxamer 188-Related Decreases in Inflammation and Tissue Damage after Experimental Brain Injury in Rats. *J. Neurosurg.* **2004**, *101*, 91−96.

(27) Nishiyama, N.; Kataoka, K. Nanostructured Devices Based on Block Copolymer Assemblies for Drug Delivery: Designing Structures for Enhanced Drug Function. *Adv. Polym. Sci.* **2006**, *193*, 67−101.

(28) Kabanov, A. V.; Nazarova, I. R.; Astafieva, I. V.; Batrakova, E. V.; Alakhov, V. Y.; Yaroslavov, A. A.; Kabanov, V. A. Micelle Formation and Solubilization of Fluorescent Probes in Poly-(oxyethylene-B-Oxypropylene-B-Oxyethylene) Solutions. *Macromolecules* **1995**, *28*, 2303−2314.

(29) Retamal, M. J.; Cisternas, M. A.; Gutierrez-Maldonado, S. E.; Perez-Acle, T.; Seifert, B.; Busch, M.; Huber, P.; Volkmann, U. G. Towards Bio-Silicon Interfaces: Formation of an Ultra-Thin Self-Hydrated Artificial Membrane Composed of Dipalmitoylphosphatidylcholine (DPPC) and Chitosan Deposited in High Vacuum from the Gas-Phase. *J. Chem. Phys.* **2014**, *141*, 104201.

(30) Wu, G.; Lee, K. Y. C. Effects of Poloxamer 188 on Phospholipid Monolayer Morphology : An Atomic Force Microscopy Study. *Society* **2009**, *25*, 2133−2139.

(31) Frey, S. L.; Lee, K. Y. C. Temperature Dependence of Poloxamer Insertion into and Squeeze-out from Lipid Monolayers. *Langmuir* **2007**, *23*, 2631−2637.

(32) Chung, H. J.; Lee, Y.; Park, T. G. Thermo-Sensitive and Biodegradable Hydrogels Based on Stereocomplexed Pluronic Multi-Block Copolymers for Controlled Protein Delivery. *J. Controlled Release* **2008**, *127*, 22−30.

(33) D'Errico, G.; Paduano, L.; Khan, A. Temperature and Concentration Effects on Supramolecular Aggregation and Phase Behavior for Poly(propylene Oxide)-B-Poly(ethylene Oxide)- B-Poly(propylene Oxide) Copolymers of Different Composition in Aqueous Mixtures, 1. *J. Colloid Interface Sci.* **2004**, *279*, 379−390.

(34) Sun, C.-Z.; Lu, C.-T.; Zhao, Y.-Z.; Guo, P.; Tian, J. L.; Zhang, L.; Li, X. K.; Lv, H. F.; Dai, D. D.; Li, X. Characterization of the Doxorubicin-Pluronic F68 Conjugate Micelles and Their Effect on Doxorubicin Resistant Human Erythroleukemic Cancer Cells. *J. Nanomed. Nanotechnol.* **2011**, *2*, 114.

(35) Yamamoto, Y.; Yasugi, K.; Harada, A.; Nagasaki, Y.; Kataoka, K. Temperature-Related Change in the Properties Relevant to Drug Delivery of Poly(ethylene Glycol)-poly(D,L-Lactide) Block Copolymer Micelles in Aqueous Milieu. *J. Controlled Release* **2002**, *82*, 359−371.

(36) Cisternas, E. A.; Corrales, T. P.; Del Campo, V.; Soza, P. A.; Volkmann, U. G.; Bai, M.; Taub, H.; Hansen, F. Y. Crystalline-to-Plastic Phase Transitions in Molecularly Thin N -Dotriacontane Films Adsorbed on Solid Surfaces. *J. Chem. Phys.* **2009**, *131*, 114705.

https://dx.doi.org/10.1021/acsomega.9b02965
ACS Omega 2020, 5, 20707−20723

(37) Bonhomme, C.; Gervais, C.; Laurencin, D. Recent NMR Developments Applied to Organic-Inorganic Materials. *Prog. Nucl. Magn. Reson. Spectrosc.* **2014**, *77*, 1−48.
(38) Foster, B.; Cosgrove, T.; Hammouda, B. Pluronic Triblock Copolymer Systems and Their Interactions with Ibuprofen. *Langmuir* **2009**, *25*, 6760−6766.
(39) Halacheva, S.; Rangelov, S.; Tsvetanov, C. Poly(glycidol)-Based Analogues to Pluronic Block Copolymers. Synthesis and Aqueous Solution Properties. *Macromolecules* **2006**, *39*, 6845−6852.
(40) Menezes, D. B.; Reyer, A.; Marletta, A.; Musso, M. Glass Transition of Polystyrene (PS) Studied by Raman Spectroscopic Investigation of Its Phenyl Functional Groups. *Mater. Res. Express* **2017**, *4*, No. 015303.
(41) González Henríquez, C. M.; Tagle, L. H.; Terraza, C. A.; Barriga González, A.; Volkmann, U. G.; Cabrera, A. L.; Ramos-Moore, E.; Pavez-Moreno, M. Structural Symmetry Breaking of Silicon-Containing Poly(amide-Imide) Oligomers and Its Relation to Electrical Conductivity and Raman-Active Vibrations. *Polym. Int.* **2012**, *61*, 197−204.
(42) Vignaud, G.; Bardeau, J.-F.; Gibaud, A.; Grohens, Y. Multiple Glass-Transition Temperatures in Thin Supported Films of Isotactic PMMA as Revealed by Enhanced Raman Scattering. *Langmuir* **2005**, *21*, 8601−8604.
(43) Oda, A.; Takahashi, O. Validation of ArgusLab Efficiencies for Binding Free Energy Calculations. *Chem-Bio Inf. J.* **2009**, *9*, 52−61.
(44) Mihajlović, M. L.; Mitrašinović, P. M. Some Novel Insights into the Binding of Oseltamivir and Zanamivir to H5N1 and N9 Influenza Virus Neuraminidases: A Homology Modeling and Flexible Docking Study. *J. Serb. Chem. Soc.* **2009**, *74*, 1−13.
(45) Tetko, I. V.; Bruneau, P. Application of ALOGPS to Predict 1-octanol/water Distribution Coefficients, logP, and logD, of AstraZeneca In-house Database. *J. Pharm. Sci.* **2004**, *93*, 3103−3110.
(46) Yu, C.; Liu, Q.; Lan, L.; Hu, B. Comparison of Dual Solvent-Stir Bars Microextraction and U-Shaped Hollow Fiber−liquid Phase Microextraction for the Analysis of Sudan Dyes in Food Samples by High-Performance Liquid Chromatography−ultraviolet/mass Spectrometry. *J. Chromatogr. A* **2008**, *1188*, 124−131.
(47) Mukherjee, S.; Bartlow, V. M.; Nair, S. Phenomenology of Growth of Single-Walled Aluminosilicate and Aluminogermanate Nanotubes of Precise Dimensions. *Chem. Mater.* **2005**, *17*, 4900−4909.
(48) Tidswell, I. M.; Ocko, B. M.; Pershan, P. S.; Wasserman, S. R.; Whitesides, G. M.; Axe, J. D. X-Ray Specular Reflection Studies of Silicon Coated by Organic Monolayers (Alkylsiloxanes). *Phys. Rev. B* **1990**, *41*, 1111−1128.
(49) Palermo, V.; Samorì, P. Molecular Self-Assembly across Multiple Length Scales. *Angew. Chem., Int. Ed.* **2007**, *46*, 4428−4432.
(50) Jin, Y. J.; Luo, Y. J.; Li, G. P.; Li, J.; Wang, Y. F.; Yang, R. Q.; Lu, W. T. Application of Photoluminescent CdS/PAMAM Nanocomposites in Fingerprint Detection. *Forensic Sci. Int.* **2008**, *179*, 34−38.
(51) Samith, V. D.; Ramos-Moore, E. Study of Glass Transition in Functionalized Poly(itaconate)s by Differential Scanning Calorimetry, Raman Spectroscopy and Thermogravimetric Analysis. *J. Non-Cryst. Solids* **2015**, *408*, 37−42.
(52) Samith, V. D.; Ruíz-Fernández, A. R.; Bahamondes-Padilla, V. E.; Muñoz-Gacitúa, D.; Ramos-Moore, E.; Davis, S. Microcanonical Molecular Dynamics Simulation of the Vitreous Phase Transition of Poly(binaphthylphosphazene). *J. Non-Cryst. Solids* **2017**, *460*, 90−97.
(53) Baptiste, A.; Bulou, A.; Bardeau, J.-F.; Nouet, J.; Gibaud, A.; Wen, K.; Hoeppener, S.; Maoz, R.; Sagiv, J. Substrate-Induced Modulation of the Raman Scattering Signals from Self-Assembled Organic Nanometric Films. *Langmuir* **2004**, *20*, 6232−6237.
(54) Liem, H. A Natural Length Scale for the Glass Transition of Conjugated Polymer Film. *J. Phys.: Condens. Matter* **2007**, *19*, 416106.
(55) Bertoldo Menezes, D.; Reyer, A.; Marletta, A.; Musso, M. Determination of the Temperatures of the Γ, β and α Relaxation Processes in Nylon 6,6 by Raman Spectroscopy. *Polymer* **2016**, *106*, 85−90.
(56) Yalkowskyx, S. H.; Valvani, S. C.; Roseman, T. J. Solubility and Partitioning VI: Octanol Solubility and Octanol−Water Partition Coefficients. *J. Pharm. Sci.* **1983**, *72*, 866−870.
(57) Wang, L.; Song, Y.; Zhang, B.; Wang, E. Adsorption Behaviors of Methanol, Ethanol, N-Butanol, N-Hexanol and N-Octanol on Mica Surface Studied by Atomic Force Microscopy. *Thin Solid Films* **2004**, *458*, 197−202.
(58) Paineu, E.; Amara, M. S.; Monet, G.; Peyre, V.; Rouzière, S.; Launois, P. Effect of ionic Strength on Bundling of Metal Oxide Imogolite Nanotubes. *J. Phys. Chem. C* **2017**, *121*, 21740−21749.
(59) Marzán, L. L.; Philipse, A. P. Synthesis of platinum nanoparticles in aqueous host dispersions of Inorganic (Imogolite) Rods. *Colloids Surf., A* **1994**, *90*, 95−109.
(60) Alexandridis, P.; Holzwarth, J. F.; Hatton, T. A. Micellization of Poly (ethy1ene Oxide) -Poly (propy1ene Oxide) -Poly (ethy1ene Oxide) Triblock Copolymers in Aqueous Solutions : Thermodynamics of Copolymer Association. *Macromolecules* **1994**, *27*, 2414−2425.
(61) Olea, A. F.; Thomas, J. K. Fluorescence Studies of the Conformational Changes of Poly(methacrylic Acid) with pH. *Macromolecules* **1989**, *22*, 1165−1169.
(62) Angelini, G.; Gasbarri, C. Polymeric Aggregates in Ionic Liquids: The Green Future of the Delivery Systems. *Curr. Drug Targets* **2015**, *16*, 1606−1611.
(63) Miño, G.; Contreras, R. Non-Electrostatic Components of Short and Strong Hydrogen Bonds Induced by Compression inside Fullerenes. *Chem. Phys. Lett.* **2010**, *486*, 119−122.
(64) Tercjak, A.; Serrano, E.; Mondragon, I. Thermally Reversible Materials Based on Thermosetting Systems Modified with Polymer Dispersed Liquid Crystals for Optoelectronic Application. *Polym. Adv. Technol.* **2006**, *17*, 835−840.
(65) Azum, N.; Rub, M. A.; Asiri, A. M. Self-Association and Micro-Environmental Properties of Sodium Salt of Ibuprofen with BRIJ-56 under the Influence of Aqueous/urea Solution. *J. Dispersion Sci. Technol.* **2017**, *38*, 96−104.
(66) Asiri, A.; Marwani, H. Green Synthesis, Characterization, Photophysical and Electrochemical Properties of Bis-Chalcones. *Int. J. Electrochem. Sci.* **2014**, *9*, 799−809.
(67) Anton, N.; Saulnier, P.; Gaillard, C.; Porcher, E.; Vrignaud, S.; Benoit, J.-P. Aqueous-Core Lipid Nanocapsules for Encapsulating Fragile Hydrophilic And/or Lipophilic Molecules. *Langmuir* **2009**, *25*, 11413−11419.
(68) Dinarello, C. A. Anti-Inflammatory Agents: Present and Future. *Cell* **2010**, *140*, 935−950.
(69) Batrakova, E. V.; Kabanov, A. V. Pluronic Block Copolymers: Evolution of Drug Delivery Concept from Inert Nanocarriers to Biological Response Modifiers. *J. Controlled Release* **2008**, *130*, 98−106.
(70) Zastre, J. A.; Jackson, J. K.; Wong, W.; Burt, H. M. P-Glycoprotein Efflux Inhibition by Amphiphilic Diblock Copolymers: Relationship between Copolymer Concentration and Substrate Hydrophobicity. *Mol. Pharmaceutics* **2008**, *5*, 643−653.
(71) Batrakova, E. V.; Li, S.; Alakhov, V. Y.; Miller, D. W.; Kabanov, A. V. Optimal Structure Requirements for Pluronic Block Copolymers in Modifying P-Glycoprotein Drug Efflux Transporter Activity in Bovine Brain Microvessel Endothelial Cells. *J. Pharmacol. Exp. Ther.* **2003**, *304*, 845−854.
(72) Rapoport, N.; Pitt, W. G.; Sun, H.; Nelson, J. L. Drug Delivery in Polymeric Micelles: From in Vitro to in Vivo. *J. Controlled Release* **2003**, *91*, 85−95.
(73) Regev, R.; Katzir, H.; Yeheskely-Hayon, D.; Eytan, G. D. Modulation of P-glycoprotein-mediated multidrug resistance by acceleration of passive drug permeation across the plasma membrane. *FEBS J.* **2007**, *274*, 6204−6214.
(74) Kohori, F.; Sakai, K.; Aoyagi, T.; Yokoyama, M.; Yamato, M.; Sakurai, Y.; Okano, T. Control of Adriamycin Cytotoxic Activity Using Thermally Responsive Polymeric Micelles Composed of poly(N-Isopropylacrylamide-Co-N,N-Dimethylacrylamide)-B-Poly-(d,l-Lactide). *Colloids Surf. B* **1999**, *16*, 195−205.

https://dx.doi.org/10.1021/acsomega.9b02965
ACS Omega 2020, 5, 20707−20723

(75) Nishiyama, N.; Kataoka, K. Nanostructured Devices Based on Block Copolymer Assemblies for Drug Delivery: Designing Structures for Enhanced Drug Function. In *Polymer Therapeutics II*; Springer-Verlag: Berlin/Heidelberg; pp 67−101.
(76) Li, Y.; Li, H.; Xiao, L.; Zhou, L.; Shentu, J.; Zhang, X.; Fan, J. Hemostatic Efficiency and Wound Healing Properties of Natural Zeolite Granules in a Lethal Rabbit Model of Complex Groin Injury. *Materials* **2012**, *5*, 2586−2596.
(77) Alakhov, V. Y.; Moskaleva, E. Y.; Batrakova, E. V.; Kabanov, A. V. Hypersensitization of Multidrug Resistant Human Ovarian Carcinoma Cells by Pluronic P85 Block Copolymer. *Bioconjugate Chem.* **1996**, *7*, 209−216.
(78) Chnari, E.; Nikitczuk, J. S.; Wang, J.; Uhrich, K. E.; Moghe, P. V. Engineered Polymeric Nanoparticles for Receptor-Targeted Blockage of Oxidized Low Density Lipoprotein Uptake and Atherogenesis in Macrophages. *Biomacromolecules* **2006**, *7*, 1796−1805.
(79) Wang, J.; Plourde, N. M.; Iverson, N.; Moghe, P. V.; Uhrich, K. E. Nanoscale Amphiphilic Macromolecules as Lipoprotein Inhibitors: The Role of Charge and Architecture. *Int. J. Nanomed.* **2007**, *2*, 697−705.
(80) Dümig, A.; Schad, P.; Kohok, M.; Beyerlein, P.; Schwimmer, W.; Kögel-Knabner, I. A Mosaic of Nonallophanic Andosols, Umbrisols and Cambisols on Rhyodacite in the Southern Brazilian Highlands. *Geoderma* **2008**, *145*, 158−173.
(81) Yamamoto, Y.; Nagasaki, Y.; Kato, Y.; Sugiyama, Y.; Kataoka, K. Long-Circulating Poly(ethylene Glycol)-poly(D,L-Lactide) Block Copolymer Micelles with Modulated Surface Charge. *J. Controlled Release* **2001**, *77*, 27−38.
(82) Ivanov, D.; Assessment of drug-loaded nanoparticles in a 3D in vitro brain tumour model Thesis. April, http//www.researchgate.net/publication/319538033, Delyan Ivanov, 2015, pp 190.
(83) Quennouz, N.; Hashmi, S. M.; Choi, H. S.; Kim, J. W.; Osuji, C. O. Rheology of Cellulose Nanofibrils in the Presence of Surfactants. *Soft Matter.* **2016**, 157. Supplementary Information, ©The Royal of Society of Chemistry

https://dx.doi.org/10.1021/acsomega.9b02965
ACS Omega 2020, 5, 20707−20723